Engineering Structures 354 (2026) 122377

Contents lists available at ScienceDirect

Engineering Structures

journal homepage: www.elsevier.com/locate/engstruct

An extended formulation of the Force Density Method accounting for bending[☆]

Ferdinando Auricchio [a], Matteo Bruggi [b],[*], Bálint Tóth [b,c]

[a] Department of Civil Engineering and Architecture, Università di Pavia, Italy
[b] Department of Civil and Environmental Engineering, Politecnico di Milano, Italy
[c] Department of Structural Mechanics, Budapest University of Technology and Economics, Hungary

ARTICLE INFO

Keywords:
Form-finding
Force density method
Gridshells
Bending resistance
Structural optimization

ABSTRACT

The Force Density Method enables the form-finding of reticulated shells by exploiting the equilibrium conditions of bar structures. An extended formulation is introduced in this contribution, tailored to gridshells that exhibit bending resistance in the vertical plane. The concept of force density is expanded to encompass not only axial forces but also bending moments and shear forces. Under this framework, it is shown that the translational equilibrium of nodes remains linear with respect to vertical coordinates, provided the gridshell has fixed footprint. A min–max problem is formulated using both sets of force densities to identify reticulated shells that satisfy equilibrium within a prescribed plan projection, while minimizing the peak reaction forces at restrained nodes. Vertical equilibrium of the unrestrained nodes is inherently satisfied, whereas horizontal equilibrium, rotational equilibrium, and total member length are enforced via equality constraints. To solve the problem, a smoothed approach is employed using a constrained minimization algorithm. Numerical simulations demonstrate that the bending capacity of the members significantly influences the equilibrium-driven form-finding of compressive gridshells. Examples are provided showing bending-resistant reticulated shells that can transmit gravity loads without requiring horizontal reactions, across different types of geometry and connectivity of the grid.

1. Introduction

Reticulated shells are structural systems characterized by a spatial network of interconnected linear elements that conform to a doubly curved surface. This configuration facilitates efficient load transfer predominantly through axial forces, thereby promoting material economy and enhancing structural legibility [1]. While funicular forms can be derived analytically, the generation of diverse geometries typically calls for computational methods. Early explorations relied on physical models (such as ropes, chains, and other flexible materials), to investigate equilibrium shapes. However, numerical techniques provide a more efficient and versatile framework for exploring the design space, enabling precise control and optimization of structural performance.

Among the various form-finding approaches discussed in the literature, see e.g. [2–8], the “Force Density Method” (FDM) [9] has achieved widespread adoption because of its algorithmic simplicity and computational efficiency. By reformulating the nodal equilibrium equations in terms of “force densities” - defined as the ratio of internal force to member length - the system becomes linear with respect to the nodal coordinates and decoupled across the three Cartesian directions. Consequently, by prescribing a set of force densities, one can generate statically admissible geometries through the solution of three linear systems, thereby enabling efficient and rapid exploration of funicular forms. Originally introduced as a conceptual design tool for pre-stressed cable networks, FDM laid the foundation for a wide range of applications and extensions. These span from cable structures and tensile membranes [10–12] to truss geometry and topology optimization [13,14], as well tensegrity systems [15–18] and compressive gridshells [19]. Recent developments include extending FDM to form-finding of adaptive truss structures under multiple loading conditions [20], as well as integrating it with energy principles to design flexible components [21]. Reference is made to [22] for a detailed understanding of the force density concept within the framework of nonlinear finite element analysis and to [23] for insights into the mathematical analogy between force density networks and electric circuits.

[☆] This article is part of a Special issue entitled: ‘Intelligent Structure’ published in Engineering Structures.

[*] Corresponding author.

E-mail addresses: ferdinando.auricchio@unipv.it (F. Auricchio), matteo.bruggi@polimi.it (M. Bruggi), toth.balint@emk.bme.hu, balint.toth@polimi.it (B. Tóth).

https://doi.org/10.1016/j.engstruct.2026.122377

The linear version of FDM does not allow for directly incorporating local enforcements, such as prescribed coordinates for unrestrained nodes or bounds on element lengths and internal forces. To address this limitation, constrained variants of the method have been developed, typically employing iterative procedures to handle the nonlinearities introduced by these additional requirements, see [11,24–26]. These include the adoption of methods of structural optimization and gradient-based minimization algorithms [27]. By adopting force densities as design variables, the sensitivity of key structural quantities can be expressed through Jacobian matrices, as originally derived in [9].

Focusing on optimal gridshell design based on equilibrium principles, FDM has been widely employed to achieve configurations with minimal thrust and efficient load paths. The concept of minimizing horizontal reactions at restrained nodes was first introduced in the context of limit analysis for masonry vaults, see e.g. [28–31]. According to [32], minimizing the total load path, defined as the sum of the absolute value of the internal force multiplied by the element length, directly correlates with minimizing structural weight within a fully stressed plastic design framework, see also [33]. A constrained version of FDM was proposed in [34], integrating total load path minimization with geometric constraints on member lengths and spatial positioning of unrestrained nodes. A min–max optimization strategy was introduced in [35] to regulate the utilization of each structural element with respect to yielding and member buckling of reticulated shells, considering manufacturing constraints in additive manufacturing.

Minimum-weight design problems under stress constraints are typically addressed within the framework of classical plastic layout optimization, which relies on the ground structure approach and assumes rigid-plastic material behavior, see e.g. [36–38]. Equilibrium-based solutions are sought while compatibility and constitutive laws are disregarded, focusing primarily on truss structures composed exclusively of axially loaded members, with very few exceptions. Reference is also made to the optimal design of tensegrity structures under bending and their connection to discrete Michell trusses, see [39, 40]. A notable extension was proposed by [41], who introduced a grillage layout optimization method considering beams subjected to pure bending, explicitly excluding axial force contributions. More recently, [42] explored plastic layout optimization for hybrid truss–beam systems in two-dimensional settings, opening new avenues for structurally versatile solutions that leverage the enhanced flexibility and efficiency offered by hybrid configurations. As highlighted in [43], bending strength represents a desirable attribute in several applications of gridshell design. However, most research addressing bending behavior in conjunction with optimal form-finding is concerned on continuum shell optimization approaches [44], rather than discrete or reticulated systems. Reference is also made to the design of bending-active gridshells, which exploit elastically bent structural elements to create complex curved geometries (see e.g. [45]), as well as to the form-finding of hybrid tensegrity structures [46]. Flexible tensegrity systems extend the classical definition of tensegrity by allowing bending and buckling of compression members [47], offering desirable features for various applications, such as metamaterial design [48].

Within this framework, the present contribution introduces an extended formulation of the Force Density Method (FDM) aimed at the form-finding of gridshells exhibiting bending resistance in the vertical plane. Building upon the notion of “force density”, the method is generalized to encompass not only axial forces but also bending moments and shear forces. The introduction of axial and shear force densities reveals that the translational equilibrium of the nodes maintains a linear relationship with the vertical coordinates, provided the footprint remains fixed. The resulting equations are embedded within an optimization framework that employs both sets of force densities as design variables. Considering fixed plan projection of the nodes, vertical translational equilibrium is utilized to determine the elevation of unrestrained nodes, while equality constraints are imposed to enforce both rotational equilibrium and horizontal translational equilibrium. The main aim of this paper is to extend the FDM formalism to account for shear contributions arising from bending resistance in the vertical plane. The proposed matrix-based approach enables efficient computation of gradients, which facilitates the incorporation of constraints into iterative methods, as originally envisioned by [9] for addressing form-finding problems with additional nonlinear constraints. In this contribution, structural optimization is employed to tackle the arising equilibrium-based problem, thereby developing a novel constrained form-finding approach (see e.g. [34] for studies on compressive networks), that is specifically designed to handle three-dimensional gridshells made of hybrid truss-beam components (see in particular [42] for the design of plane structures).

To evaluate the proposed method, a min–max optimization problem is formulated, seeking equilibrated reticulated shells of prescribed total length that minimize the magnitude of reactions at the restrained nodes. The objective is to identify layouts that promote a homogeneous distribution of reactions, ideally eliminating horizontal components. The problem is tackled using an interior-point solver [49], incorporating a smooth approximation of the max function as described in [50]. Numerical simulations demonstrate that the equilibrium-based form-finding of structural gridshells is significantly influenced by the bending capacity of the members. Illustrative examples of bending-resistant reticulated shells capable of transmitting gravity loads without requiring horizontal reactions are presented and compared against classical funicular solutions.

It should be noted that the proposed method retrieves equilibrium-based solutions while neglecting the elastic behavior of the material. As discussed in the commentary on the numerical results, the validity of these outcomes should therefore be interpreted within the framework of plastic design, see also [51] for one of the few contributions of structural topology optimization under limit analysis. Nevertheless, the proposed methodology could be extended following the approach of [20], which incorporates elastostatics of trusses within the framework of an FDM method, and [21], which exploits the principles of stationary potential energy and virtual work combined with FDM to address geometrically nonlinear elastic problems.

The remainder of the paper is organized as follows. Section 2 introduces the problem formulation, focusing on both the equilibrium equations expressed in terms of force densities and the resulting constrained optimization problem, while Appendix provides an analytical derivation of the sensitivities. Section 3 presents numerical examples to assess the effectiveness of the proposed methodology. Finally, Section 4 concludes the paper by summarizing the key findings and outlining directions for ongoing research and development.

2. Problem formulation

Fundamentals of the “force density method” (FDM) [9] are recalled in Section 2.1, dealing with the equilibrium of networks of bars that withstand the load using axial forces only. In Section 2.2, the equilibrium of gridshells that are bending-resistant in the vertical plane is dealt with. A set of shear force densities, due to bending, is introduced and used in conjunction with the axial force densities peculiar to FDM. In Section 2.3, the arising equations are embedded within a multi-constrained formulation of structural optimization for form-finding of bending-resistant reticulated shells with fixed footprint.

2.1. Equilibrium of networks of bars using the force density method (FDM)

A three-dimensional network is considered, which is made of m bars and n_s nodes. Denoting by $Oxyz$ a Cartesian reference system, the nodal coordinates are collected in the arrays $\mathbf{x}_s$, $\mathbf{y}_s$, and $\mathbf{z}_s$, for the x, y, and z axes, respectively.

The topology of the spatial network is described by the connectivity matrix $\mathbf{C}_s$. In view of the developments presented in Section 2.2, $\mathbf{C}_s$ may be written as the sum of two matrices, $\mathbf{C}_{s1}$ and $\mathbf{C}_{s2}$. The entry $C_{s1,ji}$

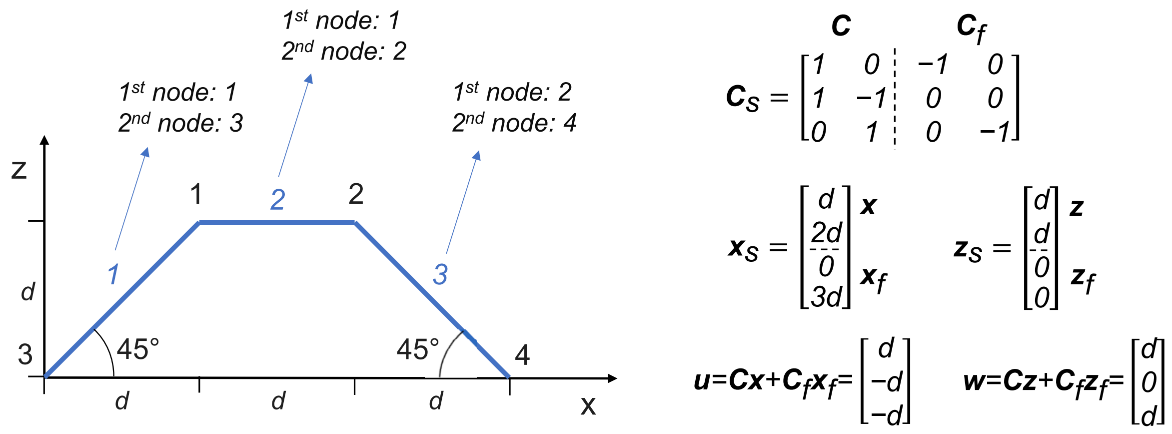

Fig. 1. A two-dimensional structure composed of three branches and four nodes, where nodes 1 and 2 are unrestrained, and nodes 3 and 4 are restrained. Derivation of **u** and **w** based on Eqs. (1).

is defined as +1, if i is the first node of the jth element; otherwise it is equal to zero. The entry $C_{s2,ji}$ is defined as −1, if i is the second node of the jth element; otherwise it is equal to zero. As in [9], the subscript s refers to the whole set of n_s nodes, the subscript f addresses the set of restrained nodes n_f, and vectors/matrices with no subscript are those of unrestrained nodes ($n = n_s - n_f$). Accordingly, the coordinates of the unrestrained and restrained nodes are stored in the arrays **x**, **y**, **z** for unrestrained nodes, and $\mathbf{x}_f$, $\mathbf{y}_f$, $\mathbf{z}_f$ for restrained nodes. The corresponding subsets of the connectivity matrix are denoted by **C** and $\mathbf{C}_f$, respectively.

The vectors **u**, **v**, **w** collect the difference in coordinates between the ends of each bar along the x, y, and z axis, respectively:

$$\mathbf{u} = \mathbf{C}_s\mathbf{x}_s = \mathbf{C}\mathbf{x}+\mathbf{C}_f\mathbf{x}_f, \quad \mathbf{v} = \mathbf{C}_s\mathbf{y}_s = \mathbf{C}\mathbf{y}+\mathbf{C}_f\mathbf{y}_f, \quad \mathbf{w} = \mathbf{C}_s\mathbf{z}_s = \mathbf{C}\mathbf{z}+\mathbf{C}_f\mathbf{z}_f, \tag{1}$$

see Fig. 1. The vector **l** gathers the bar lengths, being $l_j = \left(u_j^2 + v_j^2 + w_j^2\right)^{1/2}$ the length of the jth element. Upon introduction of $\mathbf{U} = \mathrm{diag}(\mathbf{u})$, $\mathbf{V} = \mathrm{diag}(\mathbf{v})$, $\mathbf{W} = \mathrm{diag}(\mathbf{w})$, and $\mathbf{L} = \mathrm{diag}(\mathbf{l})$, the equilibrium equations for the unrestrained nodes of the network may be written as:

$$\mathbf{C}^T\mathbf{U}\mathbf{L}^{-1}\mathbf{a} = \mathbf{p}_x, \quad \mathbf{C}^T\mathbf{V}\mathbf{L}^{-1}\mathbf{a} = \mathbf{p}_y, \quad \mathbf{C}^T\mathbf{W}\mathbf{L}^{-1}\mathbf{a} = \mathbf{p}_z, \tag{2}$$

where **a** gathers the bar forces and $\mathbf{p}_x$, $\mathbf{p}_y$, $\mathbf{p}_z$ collect the components of the point loads at the unrestrained nodes along the Cartesian axes. The jth column of the equilibrium matrices $\mathbf{C}^T\mathbf{U}\mathbf{L}^{-1}$, $\mathbf{C}^T\mathbf{V}\mathbf{L}^{-1}$ and $\mathbf{C}^T\mathbf{W}\mathbf{L}^{-1}$ have null entries, except for the indexes corresponding to the nodes of the jth bar. These entries retrieves the components of the unit vector of the axial force at the first and at the second node of the bar, $\mathbf{n}_{a,j}^{(1)}$ and $\mathbf{n}_{a,j}^{(2)}$ respectively. Indeed, for any positive (tensile) axial force acting in the jth bar, one has:

$$\mathbf{n}_{a,j}^{(1)} = -n_{x,j}\,\mathbf{e}_x - n_{y,j}\,\mathbf{e}_y - n_{z,j}\,\mathbf{e}_z = -\frac{\Delta x_j}{l_j}\,\mathbf{e}_x - \frac{\Delta y_j}{l_j}\,\mathbf{e}_y - \frac{\Delta z_j}{l_j}\,\mathbf{e}_z, \quad \mathbf{n}_{a,j}^{(2)} = -\mathbf{n}_{a,j}^{(1)}. \tag{3}$$

In the above equations, $\mathbf{e}_x$, $\mathbf{e}_y$, $\mathbf{e}_z$ are unit vectors aligned with the axes of the Cartesian reference system, $n_{x,j}$, $n_{y,j}$, $n_{z,j}$ are the direction cosines of the jth bar, and Δx_j, Δy_j, Δz_j refer to the difference in coordinates between the ends the bar, see Fig. 2(left).

In the jth bar, the so-called "force density", hereafter referred to as "axial force density", reads $q_j = a_j/l_j$. The axial force density vector collects the ratio axial force to length of the bars, i.e.:

$$\mathbf{q} = \mathbf{L}^{-1}\mathbf{a}. \tag{4}$$

Upon introduction of Eq. (4), Eqs. (2) become:

$$\mathbf{C}^T\mathbf{Q}\mathbf{C}\mathbf{x} + \mathbf{C}^T\mathbf{Q}\mathbf{C}_f\mathbf{x}_f = \mathbf{p}_x, \quad \mathbf{C}^T\mathbf{Q}\mathbf{C}\mathbf{y} + \mathbf{C}^T\mathbf{Q}\mathbf{C}_f\mathbf{y}_f = \mathbf{p}_y, \quad \mathbf{C}^T\mathbf{Q}\mathbf{C}\mathbf{z} + \mathbf{C}^T\mathbf{Q}\mathbf{C}_f\mathbf{z}_f = \mathbf{p}_z, \tag{5}$$

where $\mathbf{Q} = \mathrm{diag}(\mathbf{q})$ has been used, along with Eqs. (1). The above equations are linear in **x**, **y**, and **z**, and are uncoupled in the three directions. Hence, provided that they can be inverted, given the connectivity matrix, the load, and the coordinates of the restrained nodes, any equilibrium shape of the network is straightforwardly governed by **q**. As shown in [9], the matrix of coefficients is positive/negative definite for tensile/compressive networks without isolated points having fixed nodes that are restrained in the three directions, see also [23].

2.2. Equilibrium of reticulated shells that are bending-resistant in the vertical plane

Gridshells addressed herein are endowed with bending resistance in the vertical plane, being subjected to loads that are applied at the nodes only. In addition to the element-wise constant axial forces of funicular networks, constant shear forces and linear bending moments can arise in the members. The shear forces in the members are gathered in the vector **s**, whereas the bending moments acting at the first and second node of each element are collected in vectors $\mathbf{b}_1$ and $\mathbf{b}_2$, respectively. The adopted sign convention is such that the shear force is positive when acting upward at the first node (and downward at the second), whereas positive moment are those giving tension in the lower part of the cross-section.

The rotational equilibrium of the branches of the network implies that:

$$\mathbf{s} = \mathbf{L}^{-1}(\mathbf{b}_2 - \mathbf{b}_1), \tag{6}$$

see Fig. 2(right).

To address the translational and rotational equilibrium of the nodes, the unit vectors of the relevant bending moments and shear forces must be retrieved. The vectors of unit lengths that correspond to positive bending moments at the first and at the second node of the jth member are denoted by $\mathbf{n}_{b,j}^{(1)}$ and $\mathbf{n}_{b,j}^{(2)}$, respectively. Considering that both vectors are orthogonal to $\mathbf{e}_z$ and to the element axis, one has:

$$\mathbf{n}_{b,j}^{(1)} = -\frac{n_{y,j}}{\sqrt{n_{x,j}^2 + n_{y,j}^2}}\,\mathbf{e}_x + \frac{n_{x,j}}{\sqrt{n_{x,j}^2 + n_{y,j}^2}}\,\mathbf{e}_y, \quad \mathbf{n}_{b,j}^{(2)} = -\mathbf{n}_{b,j}^{(1)}. \tag{7}$$

For the same member, $\mathbf{n}_{s,j}^{(1)}$ and $\mathbf{n}_{s,j}^{(2)}$ are the unit vectors of the shear force at the first and at the second node. Accounting that both vectors are perpendicular to $\mathbf{n}_{b,j}^{(1)} = -\mathbf{n}_{b,j}^{(2)}$ and to the element axis, one has:

$$\mathbf{n}_{s,j}^{(1)} = -\frac{n_{x,j}\,n_{z,j}}{\sqrt{n_{x,j}^2 + n_{y,j}^2}}\,\mathbf{e}_x - \frac{n_{y,j}\,n_{z,j}}{\sqrt{n_{x,j}^2 + n_{y,j}^2}}\,\mathbf{e}_y + \frac{n_{x,j}^2 + n_{y,j}^2}{\sqrt{n_{x,j}^2 + n_{y,j}^2}}\,\mathbf{e}_z, \quad \mathbf{n}_{s,j}^{(2)} = -\mathbf{n}_{s,j}^{(1)}. \tag{8}$$

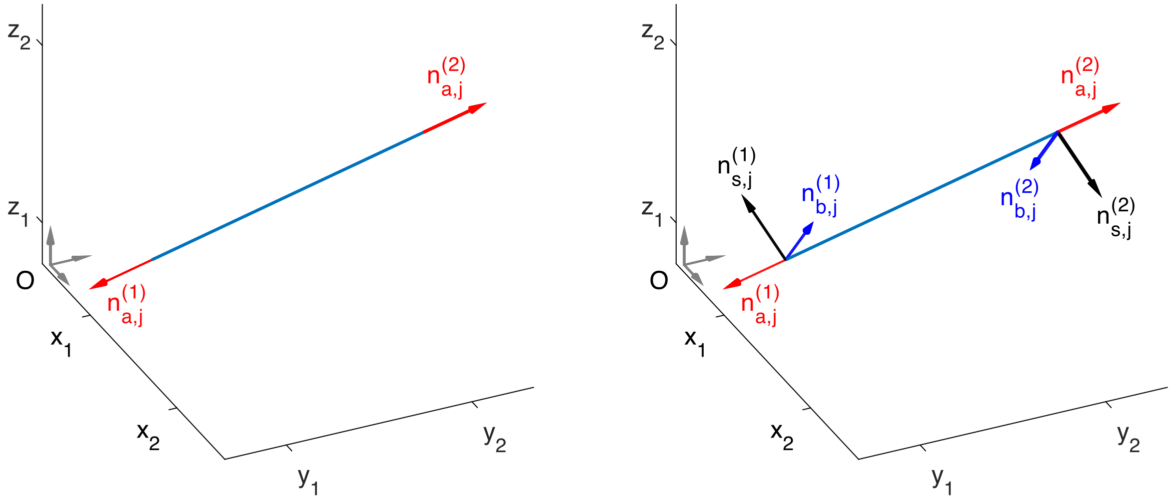

Fig. 2. Unit vectors of the internal forces at the member ends to address: networks of bars (left); reticulated shells that are bending-resistant in the vertical plane (right). Unit vectors $\mathbf{n}_{b,j}^{(1)}$ and $\mathbf{n}_{b,j}^{(2)}$ correspond to bending moments acting in the vertical plane and giving tension in the lower part of the cross-section.

Elaborating on Eqs. (3) and (8), using Eqs. (1) and (6), the translational equilibrium of the unrestrained nodes may be written as:

$$\begin{aligned}
&\mathbf{C}^T\mathbf{U}\mathbf{L}^{-1}\mathbf{a}-\mathbf{C}^T\mathbf{U}\mathbf{W}\mathbf{L}_{xy}^{-1}\mathbf{L}^{-2}(\mathbf{b}_2-\mathbf{b}_1)=\mathbf{p}_x,\\
&\mathbf{C}^T\mathbf{V}\mathbf{L}^{-1}\mathbf{a}-\mathbf{C}^T\mathbf{V}\mathbf{W}\mathbf{L}_{xy}^{-1}\mathbf{L}^{-2}(\mathbf{b}_2-\mathbf{b}_1)=\mathbf{p}_y,\\
&\mathbf{C}^T\mathbf{W}\mathbf{L}^{-1}\mathbf{a}+\mathbf{C}^T(\mathbf{U}^2+\mathbf{V}^2)\mathbf{L}_{xy}^{-1}\mathbf{L}^{-2}(\mathbf{b}_2-\mathbf{b}_1)=\mathbf{p}_z,
\end{aligned}\tag{9}$$

where $\mathbf{L}_{xy}=\mathrm{diag}(\mathbf{l}_{xy})$, being $l_{xy,j}=\left(u_j^2+v_j^2\right)^{1/2}$. Using Eqs. (1) and (7), the rotational equilibrium reads:

$$\mathbf{C}_1^T\mathbf{V}\mathbf{L}_{xy}^{-1}\mathbf{b}_1+\mathbf{C}_2^T\mathbf{V}\mathbf{L}_{xy}^{-1}\mathbf{b}_2=\mathbf{c}_x,\quad -\mathbf{C}_1^T\mathbf{U}\mathbf{L}_{xy}^{-1}\mathbf{b}_1-\mathbf{C}_2^T\mathbf{U}\mathbf{L}_{xy}^{-1}\mathbf{b}_2=\mathbf{c}_y,\tag{10}$$

where $\mathbf{c}_x$ and $\mathbf{c}_y$ collect the components, along the x and y axes respectively, of the moments applied at the unrestrained nodes. Couples about the z axis are not compatible with the equilibrium of the considered type of gridshells.

Looking at Eq. (9), two ratios can be conveniently introduced for the jth bar, i.e. $m_{1,j}=b_{1,j}/l_j^2$ and $m_{2,j}=b_{2,j}/l_j^2$. These may be regarded as "shear force densities", being $-b_{1,j}/l_j$ and $b_{2,j}/l_j$ the shear force due to $b_{1,j}$ and $b_{2,j}$, respectively, see Eq. (6). Gathering $m_{1,j}$ and $m_{2,j}$ in the vectors $\mathbf{m}_1$ and $\mathbf{m}_2$, respectively, one has:

$$\mathbf{m}_1=\mathbf{L}^{-2}\,\mathbf{b}_1,\quad \mathbf{m}_2=\mathbf{L}^{-2}\,\mathbf{b}_2.\tag{11}$$

Using Eq. (11), Eqs. (9) become:

$$\begin{aligned}
&\mathbf{C}^T\mathbf{U}\mathbf{q}-\mathbf{C}^T\mathbf{U}\mathbf{W}\mathbf{L}_{xy}^{-1}(\mathbf{m}_2-\mathbf{m}_1)=\mathbf{p}_x,\\
&\mathbf{C}^T\mathbf{V}\mathbf{q}-\mathbf{C}^T\mathbf{V}\mathbf{W}\mathbf{L}_{xy}^{-1}(\mathbf{m}_2-\mathbf{m}_1)=\mathbf{p}_y,\\
&\mathbf{C}^T\mathbf{W}\mathbf{q}+\mathbf{C}^T(\mathbf{U}^2+\mathbf{V}^2)\mathbf{L}_{xy}^{-1}(\mathbf{m}_2-\mathbf{m}_1)=\mathbf{p}_z,
\end{aligned}\tag{12}$$

whereas Eqs. (10) read:

$$\mathbf{C}_1^T\mathbf{V}\mathbf{L}_{xy}^{-1}\mathbf{L}^2\mathbf{m}_1+\mathbf{C}_2^T\mathbf{V}\mathbf{L}_{xy}^{-1}\mathbf{L}^2\mathbf{m}_2=\mathbf{c}_x,\quad -\mathbf{C}_1^T\mathbf{U}\mathbf{L}_{xy}^{-1}\mathbf{L}^2\mathbf{m}_1-\mathbf{C}_2^T\mathbf{U}\mathbf{L}_{xy}^{-1}\mathbf{L}^2\mathbf{m}_2=\mathbf{c}_y.\tag{13}$$

Eqs. (12) are not linear in the nodal coordinates, unless gridshells with fixed footprint are dealt with. Linearity can be recovered also in the case of two-dimensional structures lying in the xz or yz plane. The latter case will be disregarded hereafter, focusing on reticulated shells with fixed horizontal coordinates of the nodes, i.e. $\mathbf{x}=\bar{\mathbf{x}}$ and $\mathbf{y}=\bar{\mathbf{y}}$.

Dealing with prescribed footprint, matrices $\mathbf{U}$, $\mathbf{V}$, and $\mathbf{L}_{xy}$ have fixed entries. Using Eqs. (1), the third block of Eqs. (12), which prescribes the translational equilibrium along the vertical direction, reads:

$$\mathbf{C}^T\mathbf{Q}\mathbf{C}\mathbf{z}+\mathbf{C}^T\mathbf{Q}\mathbf{C}_f\mathbf{z}_f+\mathbf{C}^T(\mathbf{U}^2+\mathbf{V}^2)\mathbf{L}_{xy}^{-1}(\mathbf{m}_2-\mathbf{m}_1)=\mathbf{p}_z.\tag{14}$$

Given a feasible set of "axial force densities" $\mathbf{q}$ and "shear force densities" $\mathbf{m}_1$ and $\mathbf{m}_2$, Eq. (14) can be used to retrieve the vector $\mathbf{z}$ describing the form of an equilibrated gridshell. A feasible set of "force densities" is such that: (i) $\mathbf{q}$, $\mathbf{m}_1$, and $\mathbf{m}_2$ fulfill the first and the second block of Eqs. (12), i.e. the translational equilibrium of the nodes along the x and y axes, see also [13], and (ii) $\mathbf{m}_1$ and $\mathbf{m}_2$ also fulfill Eqs. (13), i.e. the rotational equilibrium of the nodes.

Linearity of the translational equilibrium with respect to the nodal elevations holds for reticulated shells with a fixed footprint (i.e., fixed horizontal coordinates of the n_s nodes), regardless of the type of restraints applied at the n_f restrained nodes. In this work, following the original formulation of the FDM in [9], restrained nodes allow reaction forces of arbitrary direction. However, the FDM equilibrium equations can be readily specialized to accommodate other types of restraints by separately considering the sets of nodes restrained in the x, y, and z directions (see, for example, the implementation in [35]).

The approach presented above could be generalized to reticulated shells with a fixed footprint that also exhibit bending resistance in the horizontal plane and torsional resistance. The resulting shear forces would generate force vectors at the ends of each member lying in the horizontal plane, with orientations depending solely on the (prescribed) direction cosines $n_{x,j}$, $n_{y,j}$ in the jth member. Their contributions would be incorporated into the first and second blocks of Eqs. (12), corresponding to the translational equilibrium of nodes along the x and y axes. Torsion could be treated analogously to axial force. The introduced bending moments and torsion would enter Eqs. (13), governing rotational equilibrium about the x and y axes, while an additional block of equations would be required to enforce rotational equilibrium about the z axis. Globally, this generalization would double the number of parameters and increase the number of constraints by n to ensure admissibility. Therefore, the remainder of this paper focuses on gridshells that are bending-resistant in the vertical plane, providing an algorithm to retrieve equilibrium-based solutions suitable for plastic design, see Section 1. The proposed approach is expected to more accurately capture the behavior of vertically loaded gridshells characterized by negligible torsional stiffness and minimal bending stiffness in the horizontal plane of their members and/or connections.

2.3. Form-finding of bending-resistant gridshells with fixed footprint

The framework presented in Section 2.2 can be straightforwardly embedded within formulations of structural optimization to address the form-finding of gridshells that are bending-resistant in the vertical plane while maintaining a fixed plan projection. Dealing with compressive gridshells, the following statement is considered:

$$\begin{cases} \min\limits_{q_j \le 0,\, m_{1,j},\, m_{2,j}} \quad f(\mathbf{q}, \mathbf{m}_1, \mathbf{m}_2, \mathbf{z}) & \text{(15a)} \\ \text{s.t.} \quad \mathbf{C}^T\mathbf{Q}\mathbf{C}\mathbf{z} + \mathbf{C}^T\mathbf{Q}\mathbf{C}_f\mathbf{z}_f + \mathbf{C}^T(\mathrm{U}^2 + \mathrm{V}^2)\mathbf{L}_{xy}^{-1}(\mathbf{m}_2 - \mathbf{m}_1) = \mathbf{p}_z, & \text{(15b)} \\ \mathbf{C}^T\mathbf{U}\mathbf{q} - \mathbf{C}^T\mathbf{U}\mathbf{W}\mathbf{L}_{xy}^{-1}(\mathbf{m}_2 - \mathbf{m}_1) = \mathbf{p}_x, & \text{(15c)} \\ \mathbf{C}^T\mathbf{V}\mathbf{q} - \mathbf{C}^T\mathbf{V}\mathbf{W}\mathbf{L}_{xy}^{-1}(\mathbf{m}_2 - \mathbf{m}_1) = \mathbf{p}_y, & \text{(15d)} \\ \mathbf{C}_1^T\mathbf{V}\mathbf{L}_{xy}^{-1}\mathbf{L}^2\mathbf{m}_1 + \mathbf{C}_2^T\mathbf{V}\mathbf{L}_{xy}^{-1}\mathbf{L}^2\mathbf{m}_2 = \mathbf{c}_x, & \text{(15e)} \\ \mathbf{C}_1^T\mathbf{U}\mathbf{L}_{xy}^{-1}\mathbf{L}^2\mathbf{m}_1 + \mathbf{C}_2^T\mathbf{U}\mathbf{L}_{xy}^{-1}\mathbf{L}^2\mathbf{m}_2 = -\mathbf{c}_y, & \text{(15f)} \\ g(\mathbf{q}, \mathbf{m}_1, \mathbf{m}_2, \mathbf{z}) = 0. & \text{(15g)} \end{cases}$$

The vectors $\mathbf{q}$, with $q_j < 0\ \forall j$, $\mathbf{m}_1$ and $\mathbf{m}_2$ gathering the “axial force densities” and the “shear force densities” make the set of the unknown parameters, known as “design variables”. The vector $\mathbf{z}$ collects the so-called “state variables”, see e.g. [27], whereas $\mathbf{x} = \bar{\mathbf{x}}$ and $\mathbf{y} = \bar{\mathbf{y}}$.

In Eq. (15b), the translational equilibrium of the unrestrained nodes in the vertical direction is used to compute the state variables related to the force densities, see Eq. (14). Feasibility of the set of design variables with respect to the translational equilibrium in the horizontal plane and to the rotational equilibrium is enforced by means of the equality constraints in Eqs. (15c–d) and Eqs. (15e–f), respectively. Reference is made to the first and the second block of Eqs. (12) and to Eqs. (13), respectively.

In Eq. (15a), f is the objective function, whereas g represents the left-hand side of a constraint, e.g. an equality constraint, both depending, in general, on the design and the state variables.

Among the different problems that may be formulated within an equilibrium-based framework, see e.g. [19,35,42], a min–max problem is considered in this contribution that aims at minimizing the magnitude of the reactions, given the total length of the network. Denoting by $r_{x,h}$, $r_{y,h}$, $r_{z,h}$ the Cartesian components of the force reaction at the hth of the n_f restrained nodes, the objective function reads:

$$f = \max_{h=1,\ldots,n_s} \left(r_{x,h}^2 + r_{y,h}^2 + r_{z,h}^2 \right)^{0.5} = \max_{h=1,\ldots,n_s} r_h = r_{max}, \tag{16}$$

whereas:

$$g = \sum_{j=1}^{m} l_j - l_{t,max}, \tag{17}$$

where $l_{t,max}$ is the prescribed total length of the network. The vectors gathering the Cartesian components of the force reactions can be straightforwardly computed from the state variables $\mathbf{z}$ and the force densities by writing the translational equilibrium of the restrained nodes, i.e.:

$$\begin{aligned} \mathbf{r}_x &= \mathbf{C}_f^T\mathbf{U}\mathbf{q} - \mathbf{C}_f^T\mathbf{U}\mathbf{W}\mathbf{L}_{xy}^{-1}(\mathbf{m}_2 - \mathbf{m}_1), \\ \mathbf{r}_y &= \mathbf{C}_f^T\mathbf{V}\mathbf{q} - \mathbf{C}_f^T\mathbf{V}\mathbf{W}\mathbf{L}_{xy}^{-1}(\mathbf{m}_2 - \mathbf{m}_1), \\ \mathbf{r}_z &= \mathbf{C}_f^T\mathbf{W}\mathbf{q} + \mathbf{C}_f^T(\mathrm{U}^2 + \mathrm{V}^2)\mathbf{L}_{xy}^{-1}(\mathbf{m}_2 - \mathbf{m}_1), \end{aligned} \tag{18}$$

see Eqs. (12), whereas g depends explicitly on $\mathbf{z}$ only, see Section 2.1.

The arising nonlinear optimization problem will be solved by means of an interior-point approach [49], primarily due to its availability in [52]. Alternative mathematical programming approaches could also be implemented, see e.g. [27,36,53] for discussions and implementations related to structural optimization in elastic and plastic design problems. Since the statement in Eq. (15) involves several sets of linear and nonlinear equality constraints, methods that enable their direct implementation should ideally be preferred. Indeed, reticulated shells satisfying Eq. (15b) are directly processed at each iteration of the optimization algorithm, while Eqs. (15c–g) are enforced as equality constraints throughout the solution procedure. The Kreisselmeier–Steinhauser aggregation function (J_{KS}) [50] is used to construct a smooth approximation of r_{max}, involving all the restrained nodes. When $\rho \ge 1$, the function:

$$J_{KS}(\mathbf{r}) = r_{max} + \frac{1}{\rho} \ln \sum_{h=1}^{n_f} e^{\rho\left(r_h - r_{max}\right)} \tag{19}$$

provides an upper bound for the maximum value r_{max} over the n_f values arranged in the vector $\mathbf{r} = [r_1\ r_2\ \ldots\ r_h\ \ldots\ r_{n_f}]^T$. Eq. (19) has been recently employed in structural optimization with linearized buckling criteria [54,55], proving effective in handling possible switching of the characteristic roots and in preserving smoothness of its derivative also in case of repeated eigenvalues. Following [56], a relatively large value of the aggregation parameter has been adopted, $\rho = 100$, preserving accuracy in the approximation of r_{max} without compromising stability of the numerical procedure.

Gradients are computed analytically elaborating on the derivation of Jacobian matrices in [9], see Appendix. Hessian matrices are computed numerically.

3. Numerical examples

A few numerical examples are addressed to test the equilibrium-based formulation presented in Section 2.3, considering funicular networks vs. bending-resistant reticulated shells for given connectivity and fixed footprint. Indeed, the formulation in Eq. (15) reduces to a form-finding procedure for spatial trusses when using $\mathbf{m}_1$ and $\mathbf{m}_2$ vectors such that $m_{1,j} = 0$ and $m_{2,j} = 0\ \forall j$. Vertical loading is considered in the examples that follow, meaning that $\mathbf{p}_x$, $\mathbf{p}_y$, $\mathbf{c}_x$, and $\mathbf{c}_y$ are vectors with null entries.

The adoption of Eq. (16) as objective function aims both at reducing the so-called “thrusts”, i.e. the horizontal components of the reaction, and at achieving an even distribution of the reactive forces at the restrained nodes. Arcuated structures are often characterized by non-negligible horizontal components of the reactions and a non homogeneous request in terms of bearing capacity of the supports. As shown next, bending resistance can be exploited in reticulated shells to mitigate both issues while preserving an arcuated geometry.

In the discussion that follows, results referred to as “FDM” layouts are funicular networks that have been found using Eq. (15) with no shear force density ($m_{1,j} = 0$ and $m_{2,j} = 0\ \forall j$), whereas “EFDM” is used to address reticulated shells with bending resistance. For the two-dimensional example presented in Section 3.1, the lower bound for the (negative) axial force densities is set to $-25\,\mathrm{kN/m}$, while the side constraints for the shear force densities in the EFDM simulations are defined as $-50\,\mathrm{kN/m} \le m_{1,j} \le 50\,\mathrm{kN/m}$ and $-50\,\mathrm{kN/m} \le m_{2,j} \le 50\,\mathrm{kN/m}$ $\forall j$, unless otherwise specified. For the three-dimensional examples discussed in Sections 3.2 and 3.3, the lower bound for the (negative) axial force densities is set to $-10\,\mathrm{kN/m}$, while $-10\,\mathrm{kN/m} \le m_{1,j} \le 10\,\mathrm{kN/m}$ and $-10\,\mathrm{kN/m} \le m_{2,j} \le 10\,\mathrm{kN/m}\ \forall j$ is used in the EFDM simulations, unless stated otherwise. In each optimization run, the initial guess for the minimization variables (i.e. the force densities) is chosen as the average of the corresponding lower and upper bounds. The initial values of the state variables (i.e. the vertical coordinates of the nodes) are computed by inverting Eq. (15b), using the initial values of the design unknowns. Vector plots of the force reactions and diagrams of the internal forces, i.e. axial force N (in kN), shear force V (in kN), and bending moment M (in kNm), are given. The same scaling factor is used to illustrate results for the same example (when representing the magnitude of the vector reactions and plotting diagrams for the same type of internal force). For the considered numerical tests, the main input parameters and significant output values of reactions and internal forces are summarized in Table 1.

Table 1
Main input parameters and significant output values of reactions and internal forces for the optimal FDM/EFDM layouts presented in Section 3: length in footprint of the network $l_{t,0}$, prescribed total length of the network $l_{t,max}$, resultant of the applied vertical load P, peak value of the force reaction r_{max}, value of the objective function at convergence f_c, peak value of the horizontal component of the force reaction (thrust) $r_{h,max}$, peak value of the compressive axial force N_{max}, shear force V_{max}, and bending moment M_{max}.

	$l_{t,0}$ (m)	$l_{t,max}$ (m)	P (kN)	r_{max} (kN)	f_c (kN)	$r_{h,max}$ (kN)	N_{max} (kN)	V_{max} (kN)	M_{max} (kNm)
Section 3.1									
FDM - Fig. 3	4	6	15	8.45	8.45	3.89	8.45	–	–
EFDM - Fig. 4	4	6	15	7.50	7.50	0.00	3.84	6.80	8.00
EFDM - Fig. 5(left)	4	6	15	8.24	8.24	3.42	7.98	2.08	1.68
EFDM - Fig. 5(right)	4	6	15	8.31	8.31	3.58	7.97	2.34	2.00
Section 3.2									
FDM - Fig. 6	220	253	121	4.12	4.13	3.76	4.12	–	–
EFDM - Fig. 7	220	253	121	2.75	2.76	0.00	2.41	2.73	7.64
EFDM - Fig. 9(left)	220	253	121	3.48	3.49	2.78	3.48	1.46	2.70
EFDM - Fig. 9(right)	220	253	121	3.68	3.68	3.12	3.68	1.11	1.76
Section 3.3									
FDM - Fig. 13	251.31	289	72.13	9.06	9.06	7.86	8.30	–	–
EFDM - Fig. 14	251.31	289	72.13	4.51	4.51	0.00	1.08	2.01	3.33
FDM - Fig. 15	223.82	257.39	68.72	8.13	8.14	6.91	7.35	–	–
EFDM - Fig. 16	223.82	257.39	68.72	4.30	4.30	0.00	1.46	1.60	(−)26.50

Table 2
Design of a single arch with FDM/EFDM: prescribed x-coordinates (in m) and sets of computed z-coordinates (in m) for the achieved optimal solutions (due to symmetry, only the nodes in the left half of the arch are considered).

(all Figures)	x_1 −2	x_2 −1.75	x_3 −1.50	x_4 −1.25	x_5 −1	x_6 −0.75	x_7 −0.50	x_8 −0.25	x_9 0
	z_1	z_2	z_3	z_4	z_5	z_6	z_7	z_8	z_9
FDM - Fig. 3	0	0.48	0.90	1.25	1.54	1.77	1.93	2.03	2.06
EFDM - Fig. 4	0	0.12	0.29	0.53	0.82	1.14	1.47	1.81	2.17
EFDM - Fig. 5(left)	0	0.31	0.61	0.94	1.26	1.59	1.87	2.09	2.19
EFDM - Fig. 5(right)	0	0.28	0.56	0.84	1.12	1.40	1.68	1.96	2.24

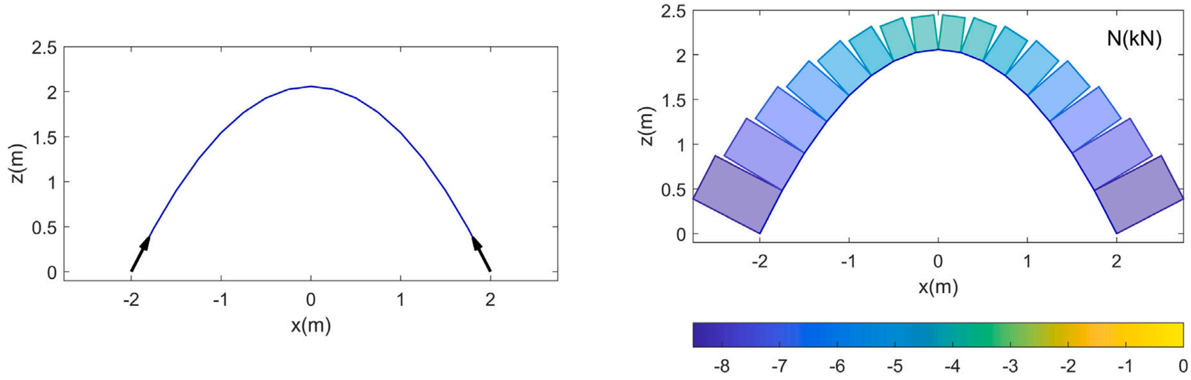

Fig. 3. FDM design of a single arch: shape, reactions and axial force diagram.

It is remarked that all the layouts presented next fulfill the enforced set of constraints (within the prescribed tolerance of 10^{-6}), i.e. they are equilibrium-based solutions to the form-finding problem.

3.1. A single arch

At first, a two-dimensional example is considered working in the x-z plane. The optimal shape of an arch is investigated, considering a structure made of $m = 16$ branches and $n_s = 17$ nodes. The two nodes at the end of the arch are restrained in both directions, whereas a vertical load $p_{z,j} = -1$ kN is applied at each one of the $n = 15$ inner unstrained nodes. The resultant of the vertical load is $P = 15$ kN, acting downward. The three-dimensional implementation of FDM/EFDM presented above is tested by seeking sets of optimal z-coordinates for the unrestrained nodes, while the x-coordinates remain prescribed. Each one of the branches has (fixed) length in footprint that equals 0.25 m. Anti-funicular polygons are sought that minimize the magnitude of the reactions at the supports with a total length $l_{t,max} = 1.5\, l_{t,0}$, being $l_{t,0} = 4$ m the length in footprint of the arch. Table 2 reports the prescribed x-coordinates and the computed z-coordinates for the optimal solutions presented in this section. The FDM layout, i.e. the results found from the solution of Eq. (15) admitting axial force densities only, is given in Fig. 3(left). Each branches behaves like a bar, implying that force reactions at support are aligned with the segments stemming from the restrained nodes, see the black arrows in the picture. According to the diagram of the axial forces represented in Fig. 3(right) the magnitude of the compressive force monotonically increases from the key of the arch to the supports, where it equals the magnitude of the reactive forces (8.45 kN).

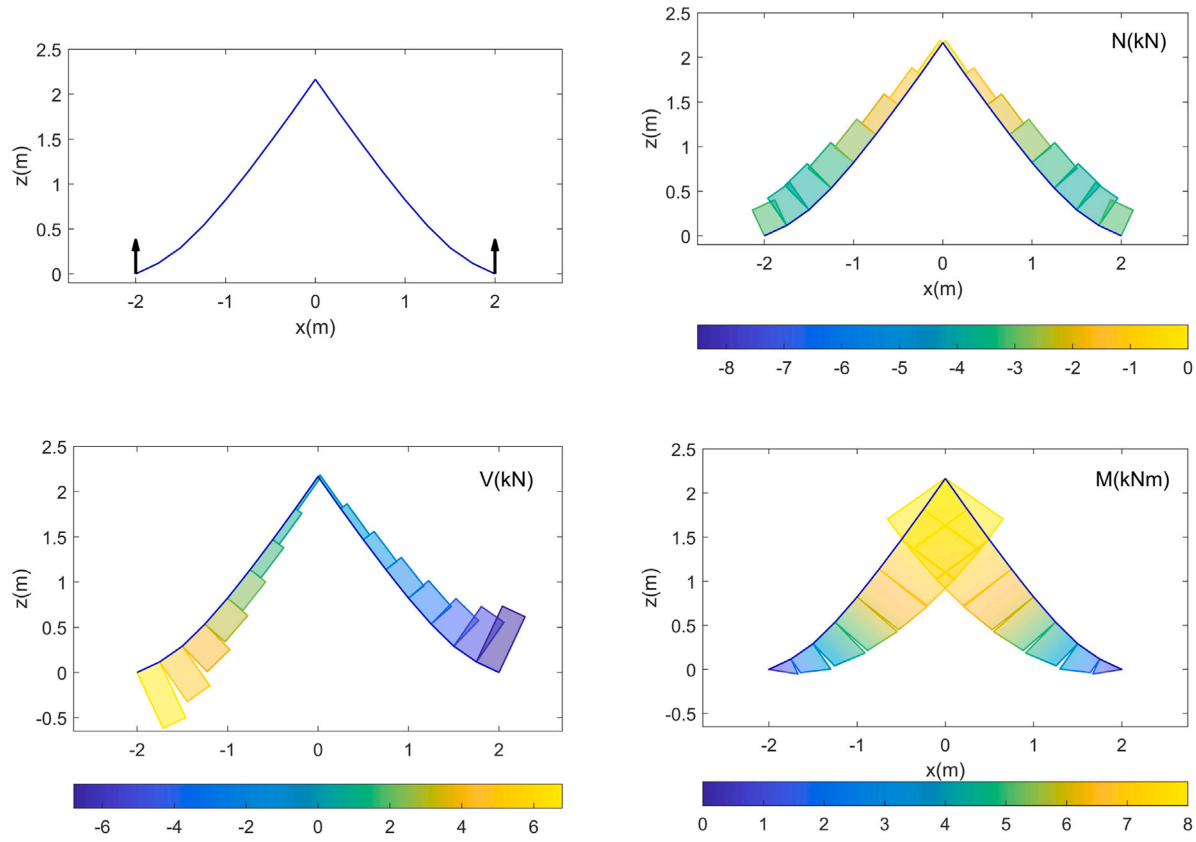

Fig. 4. EFDM design of a single arch: shape, reactions and internal force diagram.

Then, Eq. (15) is run allowing both for axial force densities and shear force densities. Hinge supports are prescribed enforcing that $m_{1,j} = 0$ and $m_{2,j} = 0$ if the relevant end of the j-bar is one of the two unrestrained nodes. The EFDM result is the hybrid truss-beam structure depicted in Fig. 4, along with the diagrams of the internal forces, i.e. axial force, shear force and bending moment. Although the FDM and the EFDM layouts have the same total length $l_{t,max}$ and a similar height of the mid-span node, their structural behavior and shape are quite different. In the EFDM layout, the shear forces acting in the branches stemming from the support allows for the arsing of a no thrust solution, where each one of the two (vertical) reactions is half of the magnitude of the total load (7.50 kN). Overall, a mixed hybrid truss-beam behavior is reported. The diagram of the axial force is non-trivial, with the largest compressive forces (3.84 kN) arising two elements far from the supports. The magnitude of the shear force monotonically decreases from the hinge supports to the mid-span node, whereas the bending moment increases from zero to its maximum value (8 kNm, as per the rotational equilibrium of half of the structure). The continuity of the bending moment across the nodes connecting adjacent branches confirms that the entries of $\mathbf{m}_1$ and $\mathbf{m}_2$ fulfill, at convergence, the rotational equilibrium of (the first block) of Eqs. (13).

Working with side constraints for the shear force densities, i.e. operating on bounds of the design variables in $\mathbf{m}_1$ and $\mathbf{m}_2$, one can tune the flexural capacity of the structure under investigation. Recalling that $m_{1,j} = b_{1,j}/l_j^2$ and $m_{2,j} = b_{2,j}/l_j^2$, the magnitude of the bending moment can be limited in each branch. The picture in Fig. 5(left) refers to an hybrid truss-beam structure that was found using a threshold equal to 10 kN/m for the unrestrained nodes of each element. The limited bending resistance does not allow for the arising of a no-thrust solution, but remarkably affects the overall shape. The picture in Fig. 5(right) is concerned with a three-hinge layout, whose internal hinge was prescribed by enforcing $m_{1,j} = 0$ and $m_{2,j} = 0$ at mid-span. In terms of magnitude of the reactions, the former solution performs marginally better than the latter.

A preliminary assessment of the numerical implementation of the method in three dimensions was done by replicating the above results after rotations of the geometry around the z axis.

3.2. An arch grid

A system of parallel arches running in two orthogonal direction is considered, see e.g. [57]. The arch grid has a square footprint with side 10 m. Each one of the arches is made of 12 branches with (fixed) length in footprint equal to 0.833 m. The nodes along the perimeter are restrained in the three directions, whereas a vertical load $p_{z,j} = -1$ kN is applied at each one of the $n = 121$ inner unstrained nodes. The resultant of the vertical load is $P = 121$ kN, downward. Gridshells whose total length is $l_{t,max} = 1.15\, l_{t,0}$ are sought. The FDM layout achieved by using Eq. (15) with $m_{1,j} = 0$ and $m_{2,j} = 0\ \forall j$ is represented in Fig. 6(left), along with a vector plot of the reactions at the supports. The optimal anti-funicular network consists of a system of arches whose rise smoothly increases as it approaches the keystone. The ratio of the horizontal to vertical component of the reaction decreases accordingly, whereas the magnitude is the same. In Fig. 6(right), the axial force diagram is represented. The maximum value is found at the support, where the axial force equals 4.12 kN in all the branches, whereas smaller forces arise at the top. The lowest compressive force equals 2.54 kN.

Then, bending-resistant reticulated shells are investigated by using Eq. (15) combined with prescription $m_{1,j} = 0$ and $m_{2,j} = 0$ if the relevant end of the j-bar is one of the restrained nodes along the perimeters. The EFDM solution resulting in the minimization of the maximum reaction magnitude is that represented in Fig. 7, along with a vector plot of the reactions and the diagrams of the axial force, the shear force and the bending moment. It is a no-thrust reticulated shell whose vertical

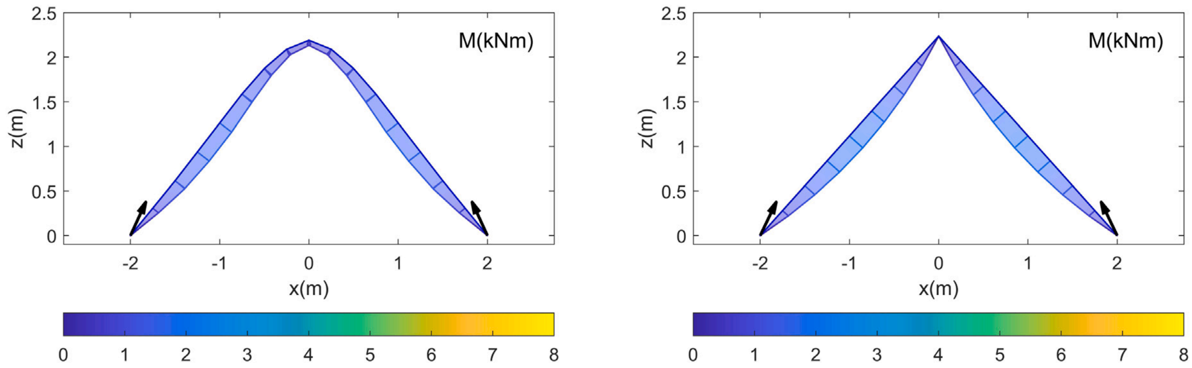

Fig. 5. EFDM design of a single arch with side constraints: shape, reactions and bending moment diagram, bounding $m_{1,j}$ and $m_{2,j}$ all over the structure (left), and prescribing an internal hinge at mid-span (right).

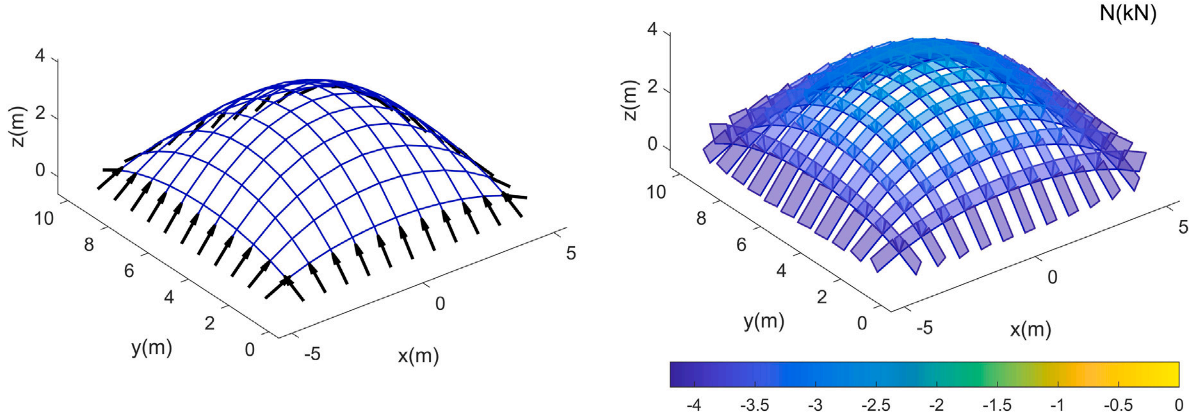

Fig. 6. FDM design of an arch grid: shape, reactions and axial force diagram.

reactions are all equals to 2.75 kN, which is the resultant of the applied load divided by the number of point supports.

Although both solutions were generated using the same total length condition, the optimal shape represented in Fig. 7 is quite different from the FDM layout depicted in Fig. 6. The parallel arches made of hybrid truss-beam elements are characterized by pointed features, recalling the geometry represented in Fig. 4. The resulting three-dimensional system consists of double-curvature portions which are connected through sharp edges. Looking at the diagrams of the internal forces along the parallel arches, the maximum shear action is generally found at the supports, whereas the regions of maximum bending moments are those at mid-span. Maximum axial forces (2.41 kN) occur at the springer of the central arches, i.e. those lying along the principal axes of the footprint as well as a few adjacent ones. The same branches exhibit the lowest shear forces compared to the other perimeter elements.

Because of Eqs. (15b-f), the internal forces and moments shown in Fig. 7 represent an equilibrated solution. Since compatibility and the constitutive law are disregarded, this solution does not necessarily coincide with the linear elastic one, unless a statically determinate structure is considered (see, for example, the three-hinge layout in Fig. 5, right). Assuming a perfectly plastic model with an associated flow rule and a satisfied yield condition, meaning that the cross-section stresses lie inside or on the yield surface in stress space, the resulting solution can be regarded as statically admissible, that is, a safe solution according to the lower-bound theorem of plasticity [27,36,51].

To provide a preliminary assessment of the results presented in Fig. 7 and discuss their implications for applicability, a finite element model of the EFDM optimal layout was built using commercial software [58]. Structural steel (S275) and IPE 240 cross-sections were adopted for all members of the network, with the web oriented vertically. End releases were introduced to model connections that do not allow the transfer of torsion and moments in the horizontal loading plane. First, a linear elastic solution was computed, applying vertical forces of -1 kN at the n inner nodes and point forces of 2.75 kN at the n_f nodes along the perimeter (i.e. the vertical reactions computed in the EFDM solution). In Fig. 8 the bending moments retrieved from the finite element solution are shown: a color map of the entire structure is provided along with the bending moment diagram for half of the outer and central arches. A very good agreement was observed between the EFDM result (maximum value 7.64 kNm) and the finite element analysis (maximum value 7.69 kNm).

A further investigation was carried out using the same model, replacing the point forces applied at the nodes along the perimeter with vertical cut-off bars having a compression threshold of 2.75 kN and ductile behavior. These elements behave as elastic struts below the limit and provide a perfectly plastic response above it. A nonlinear static analysis was then performed by gradually applying the point forces at the inner nodes. This approach allowed simulating the plastic redistribution of reaction forces across the cut-off bars, ultimately recovering the same results shown in Fig. 8. Hence, the internal forces and moments given in Fig. 7 can be interpreted as the stress state of the gridshell supported by ductile restraints that can transmit vertical forces exclusively, subject to an imposed compression limit.

Intermediate EFDM solutions can be generated operating on the side constraints of the design variables in $\mathbf{m}_1$ and $\mathbf{m}_2$. In Fig. 9(left) an hybrid truss-beam structure is shown that was found using a threshold equal to 3 kN/m for $m_{1,j}$ and $m_{2,j}l$ at the unrestrained nodes of each element. For the layout depicted in Fig. 9(right), the upper bound was instead set to 2 kN/m. In the former case, all the reactions equal 3.48kN, the axial force lies within the range of 1.61 -3.48 kN, and

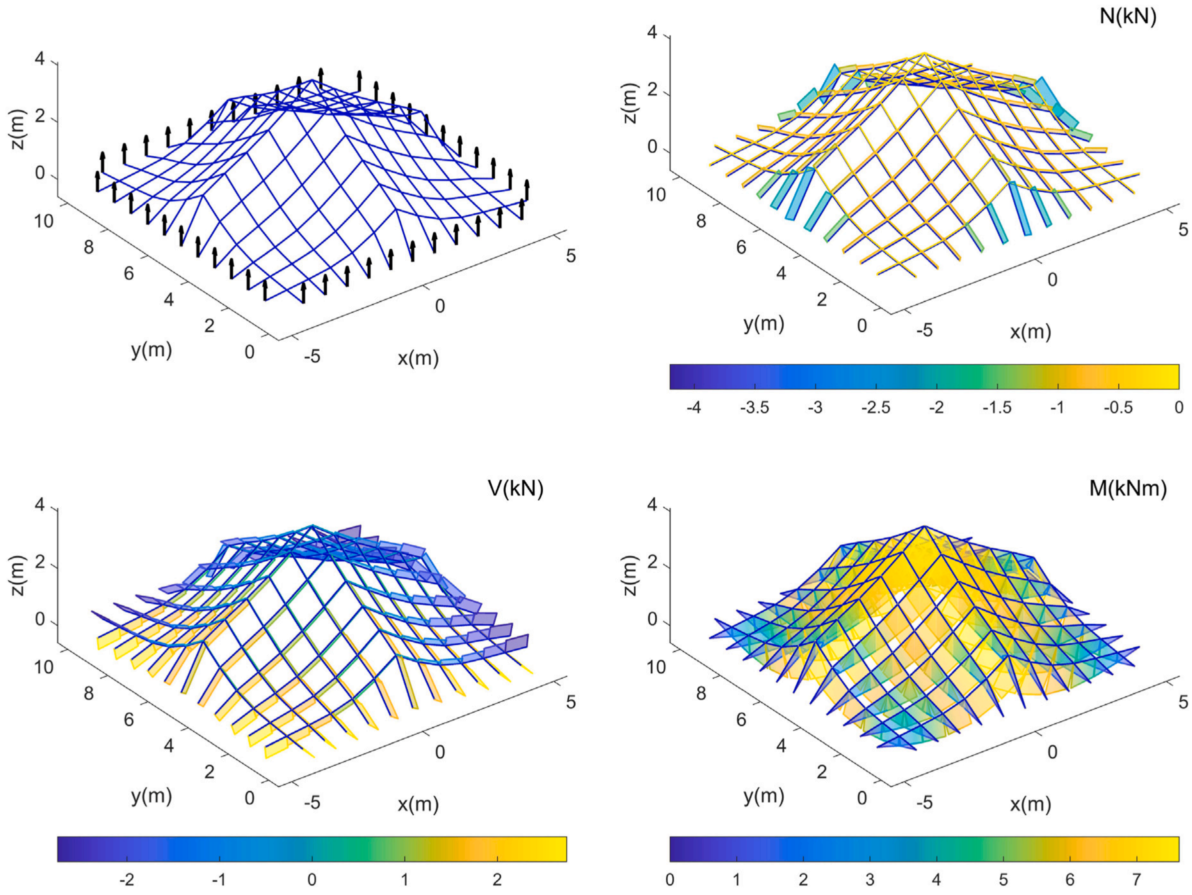

Fig. 7. EFDM design of an arch grid: shape, reactions and internal force diagram.

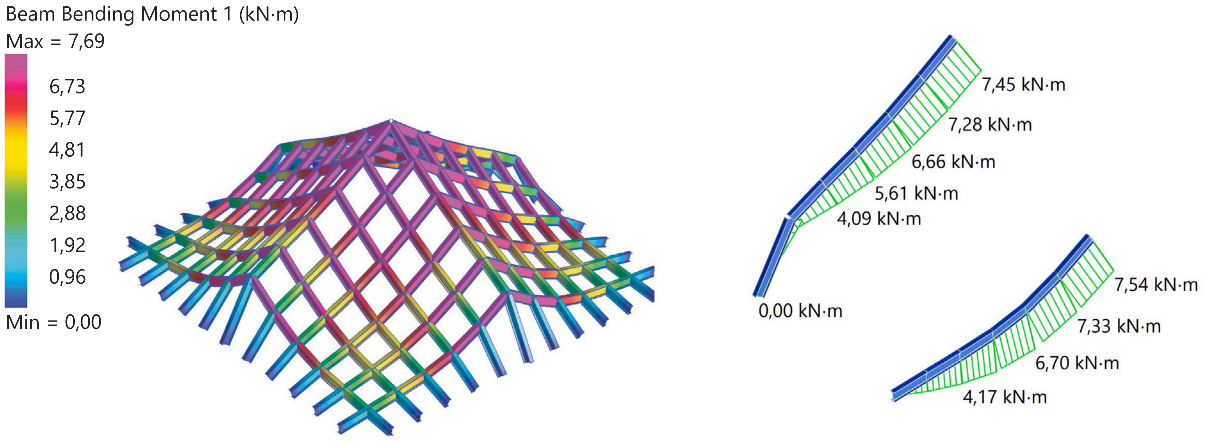

Fig. 8. EFDM design of an arch grid: bending moment representation (color map for the structure and diagram for two parts), as obtained through finite-element analysis.

the maximum bending moment equals 2.70kN. In the latter, all the reactions equal 3.68kN, the axial force varies from 2.02 kN to 3.68 kN, and the maximum bending moment is 1.76kN.

It is remarked that both the FDM shape (see Fig. 6) and the three EFDM layouts (see Fig. 7 and the two pictures in Fig. 9) are characterized by reactions that are all equal at the supports (within a tolerance of $\pm 10^{-3}$ kN). This means that, at convergence, the vector $\mathbf{r}$ in Eq. (16) is made of n_f "repeated values" that were effectively handled by the adopted smooth aggregation function, see in particular [56]. The history plots of the objective function f and of the feasibility of the constraints, i.e. the highest value among the right-hand side entries of the enforcements in Eqs. (15c–g), are represented in Fig. 10. The picture on the left refers to the generation of the FDM layout in Fig. 6, whereas that on the right is concerned with the EFDM design found using the side constraints $m_{1,j} \leq 2\,\text{kN/m}$ and $m_{2,j} \leq 2\,\text{kN/m}$ at the unrestrained nodes. In both cases, the initial guess for the minimization variables does not satisfy the equality constraints, as indicated by the initial feasibility values being greater than zero. Nonetheless, the minimization algorithm requires only a few iterations to reach the feasible design region. During the first iterations, constraint feasibility improves at the expense of an increase in the objective function; subsequently, the objective function gradually decreases toward an optimum where all

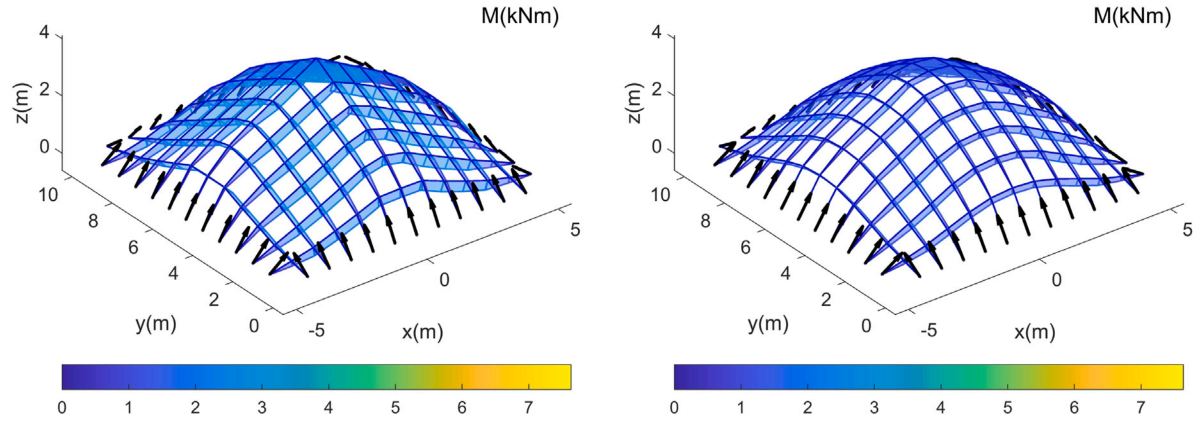

Fig. 9. EFDM design of an arch grid with side constraints: shape, reactions and bending moment diagram, bounding $m_{1,j}$ and $m_{2,j}$ all over the structure at 3 kN/m (left), and 2 kN/m (right).

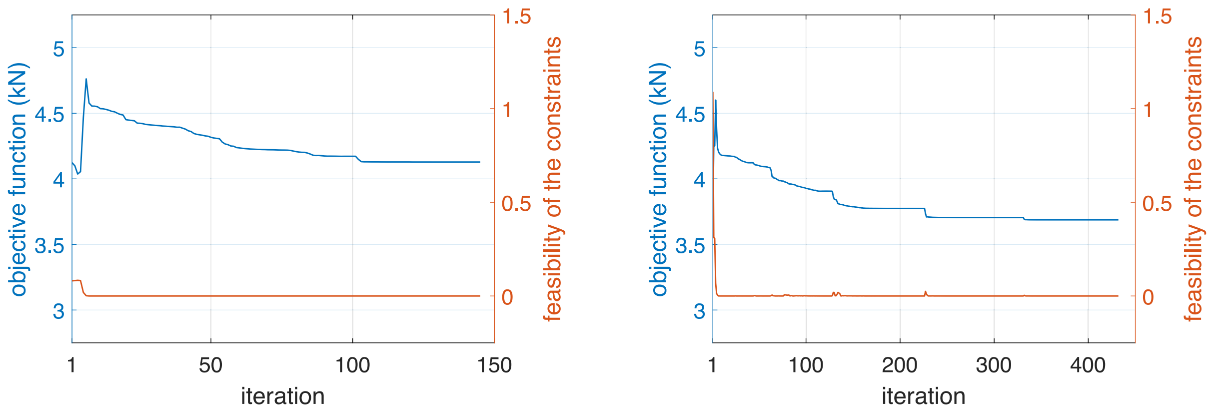

Fig. 10. Design of an arch grid: history of the objective function and of the feasibility of the constraints using FDM (left), and EFDM with side constraints $m_{1,j} \leq 2$ kN/m and $m_{2,j} \leq 2$ kN/m at the unrestrained nodes (right).

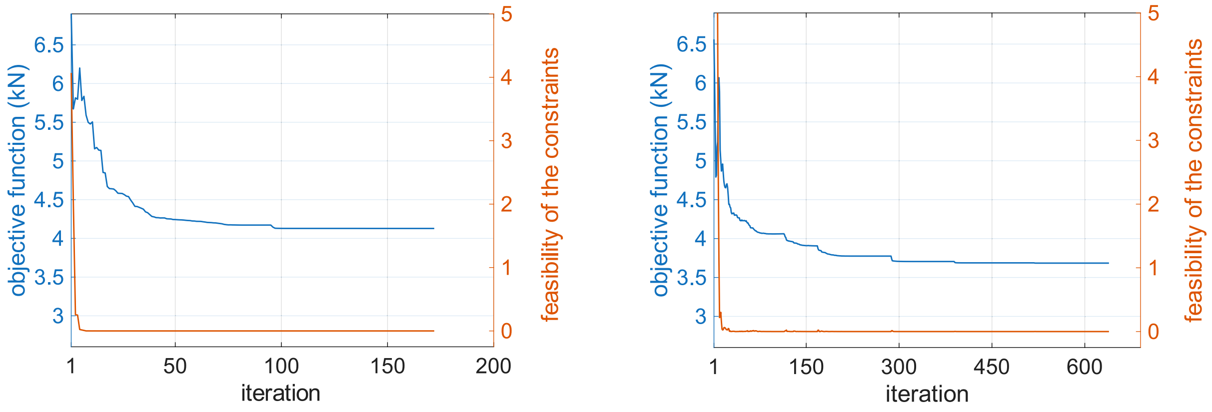

Fig. 11. Design of an arch grid with random initialization of the minimization unknowns: history of the objective function and of the feasibility of the constraints using FDM (left), and EFDM with side constraints $m_{1,j} \leq 2$ kN/m and $m_{2,j} \leq 2$ kN/m at the unrestrained nodes (right).

constraints remain satisfied. However, the EFDM approach introduces a greater number of constraints (to enforce rotational equilibrium at the nodes for non-zero $m_{1,j}$ and $m_{2,j}$), which in turn demands a higher number of iterations to ensure convergence. Apart from the total length constraint in Eq. (15g), the total number of equality constraints in the FDM optimization is $2 \cdot n = 242$, see Eq. (15c–d), whereas in the EFDM run it is $4 \cdot n = 484$, see Eq. (15c–f).

The investigation was repeated using a random initialization of the design parameters within their respective lower and upper bounds, rather than adopting the average values as the initial guess. The history plots of the objective function and the constraint feasibility are shown in Fig. 11. The figure on the left corresponds to the FDM design, while the one on the right refers to the EFDM design obtained by imposing $m_{1,j} \leq 2$ kN/m and $m_{2,j} \leq 2$ kN/m at the unrestrained nodes. The resulting solutions match those previously reported in Fig. 6 and in

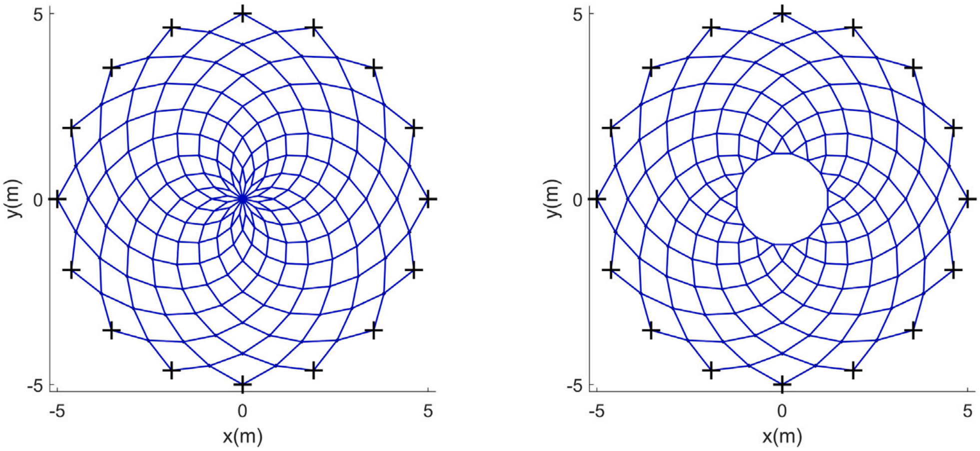

Fig. 12. Grids used in the design of a gridshell dome (left) and a gridshell dome with oculus (right).

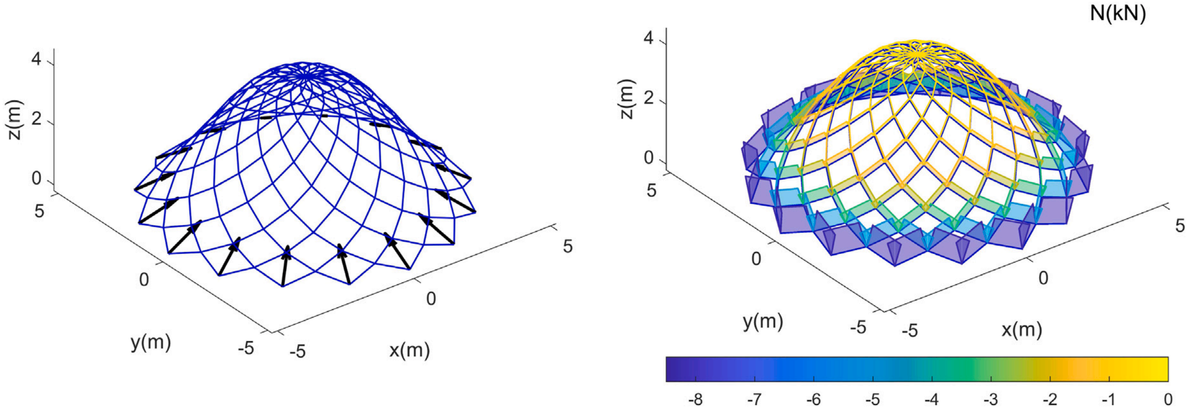

Fig. 13. FDM design of a gridshell dome: shape, reactions and axial force diagram.

Fig. 9(right), respectively (and their corresponding objective function values at convergence are identical). However, a larger number of iterations was required to achieve convergence compared to the previous optimization runs. Due to the nonlinearity of the optimization problem considered herein, the obtained solutions should generally be regarded as local minima. It is worth noting that, regardless of the type of optimality, every feasible solution achieved through Eq. (15) satisfies the equilibrium constraints and, provided the yield condition is fulfilled, corresponds to an admissible stress state within the framework of limit analysis.

3.3. A dome

A gridshell dome spanning an area with radius equal to 5 m is considered. The connectivity of a so-called “lamella” dome is investigated, as represented in Fig. 12(left), see e.g. [59,60]. The vertical load per unit of plan projection is 1 kN/m^2. All the nodes along the perimeter are restrained in the three Cartesian axes. Point loads for the inner unrestrained nodes are computed accounting for their tributary area. The resultant of the applied vertical loads reads $P = 72.13$ kN. Gridshells are sought whose total length is $l_{t,max} = 1.15\, l_{t,0}$.

At first, Eq. (15) is used prescribing $m_{1,j} = 0$ and $m_{2,j} = 0$ across all the branches of the reticulated shell. The FDM gridshell dome is depicted in Fig. 13(left), along with a vector plot of the support reactions, whereas the axial force diagram is represented in Fig. 13(right). The axial force increases from the top of the structure toward the supports. At each restrained node, the reaction equals the resultant of the axial forces acting in the two connected branches. Its magnitude is 9.06 kN. The ratio of the horizontal (radial) thrust to the vertical reaction force is 1.74.

Then, Eq. (15) is used prescribing $m_{1,j} = 0$ and $m_{2,j} = 0$ only if the relevant end of the j-bar is located at an unrestrained node. The achieved EFDM layout is that represented in Fig. 14, along with a vector plot of the reactions and the diagrams of the axial force, the shear force and the bending moment. The bending-resistant pointed dome carries the vertical load without requiring thrust at the supports. All the reactions equal 4.51 kN, which is the resultant of the applied load divided by the number of supports. As in the diagram in Fig. 13(right), the axial forces increases from top to bottom, but the compressive force magnitudes of the EFDM solution are significantly lower. The shear forces also increase from the top of the structure toward the supports, reaching peak values nearly twice as large as the maximum axial force. As for the bending moment diagram, sagging moments are present throughout the branches. Peak values occur in the first half of the dome, beyond the elements that span from the supports, whereas the values at the tip are nearly half as large.

It is noted that the radial symmetry of the reticulated shells shown in both Figs. 13 and 14 emerges as a result of numerical optimization, without any a priori geometric prescription.

A final set of investigations is carried out on a gridshell dome with an oculus, i.e. incorporating a free edge, see [43]. The connectivity of the reticulated shell is shown in Fig. 12 (right). With respect to the “lamella” dome in Fig. 12(left), a central circular hole with a radius of 1.25 m is introduced, and hoop elements are added along the

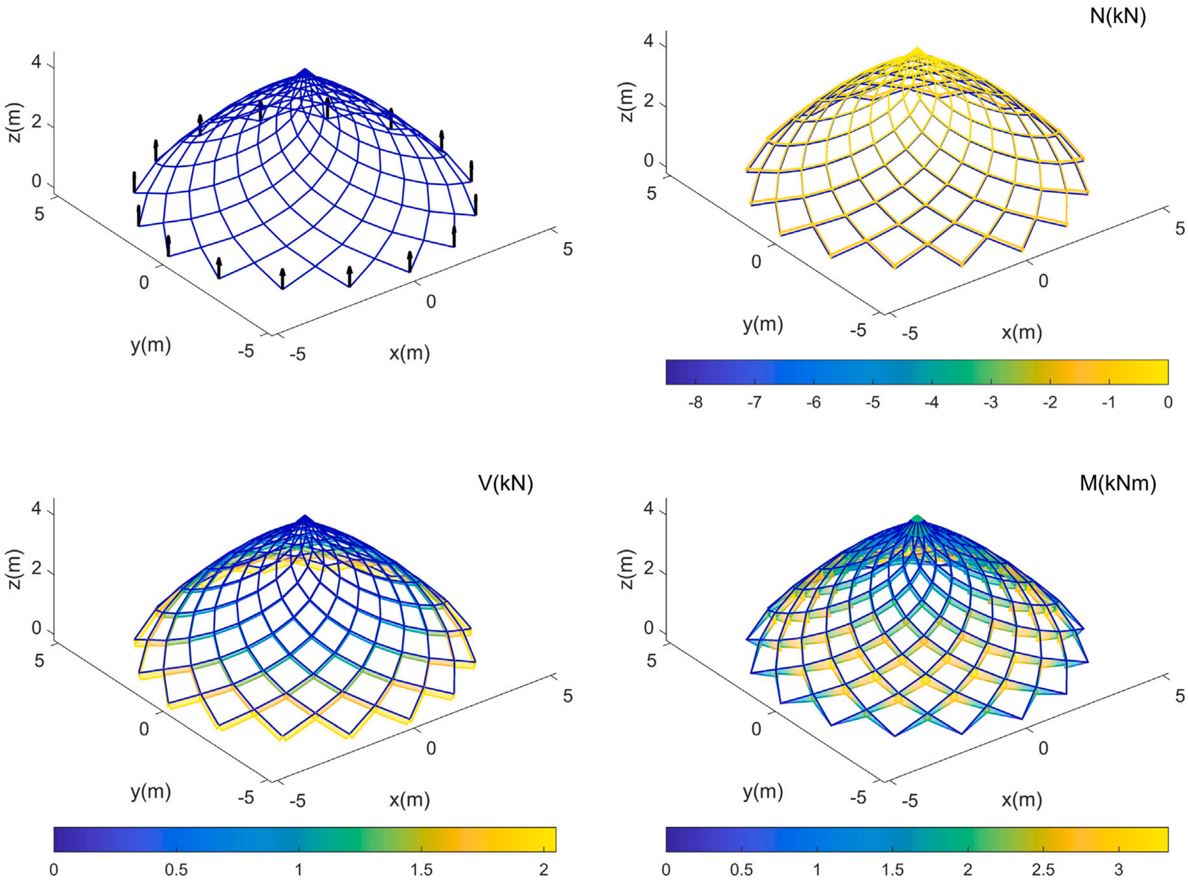

Fig. 14. FDM design of a gridshell dome: shape, reactions and axial force diagram.

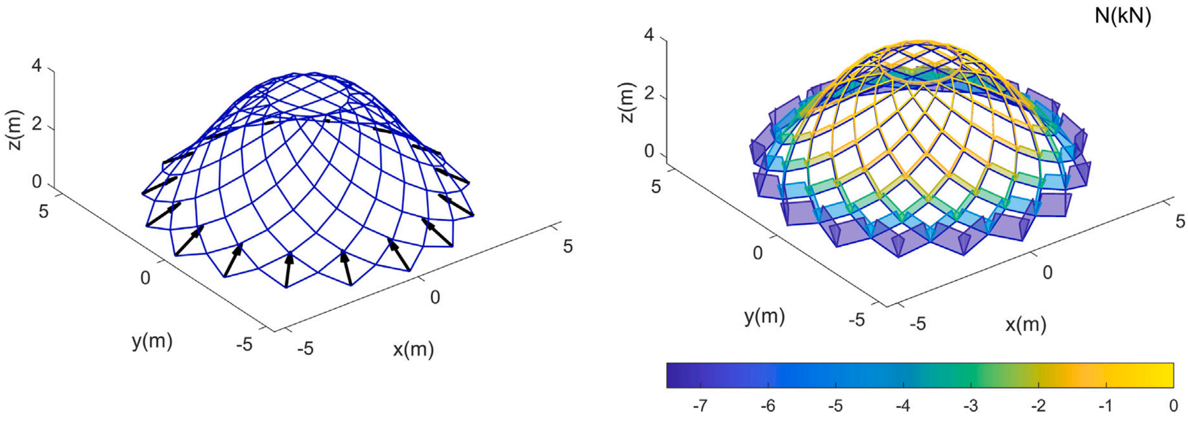

Fig. 15. FDM design of a gridshell dome with oculus: shape, reactions and axial force diagram.

perimeter of the cavity. The restrained nodes are those lying along the outer perimeter, i.e. those located along the circumference of radius 5 m meters and center at the origin. As for the gridshell dome, the vertical load per unit of plan projection is $1\,\mathrm{kN/m^2}$, with a resultant equal to $P = 68.72\,\mathrm{kN}$. Gridshells are designed to have a total length $l_{t,max} = 1.15\, l_{t,0}$.

The FDM gridshell dome depicted in Fig. 15 was found by applying Eq. (15), with $m_{1,j} = 0$ and $m_{2,j} = 0$ imposed on all branches. The diagram of the axial force in the inclined branches, see Fig. 15(right), is very similar to that represented in Fig. 13(right). The hoop elements located at the cavity boundary are subjected to compressive forces of 1.25 kN. At each restrained node, the horizontal (radial) thrust is 1.61 times the vertical reaction force, with the reaction magnitude equal to 8.13 kN.

The presence of the oculus prevents bending-resistant reticulated shells pinned to the ground from achieving a significant reduction in reaction magnitudes. Therefore, Eq. (15) is applied permitting non-zero values of $m_{1,j}$ and $m_{2,j}$ at both restrained and unrestrained nodes, i.e. searching among bending-resistant gridshells with fixed (clamped) boundary conditions at the base. The achieved EFDM layout is represented in Fig. 16. It supports the vertical load without requiring thrust at the supports, though this comes at the expense of developing moment reactions. At the restrained nodes, axial forces of 1.46 kN and shear forces of 1.60 kN combine to produce vertical reactions uniformly

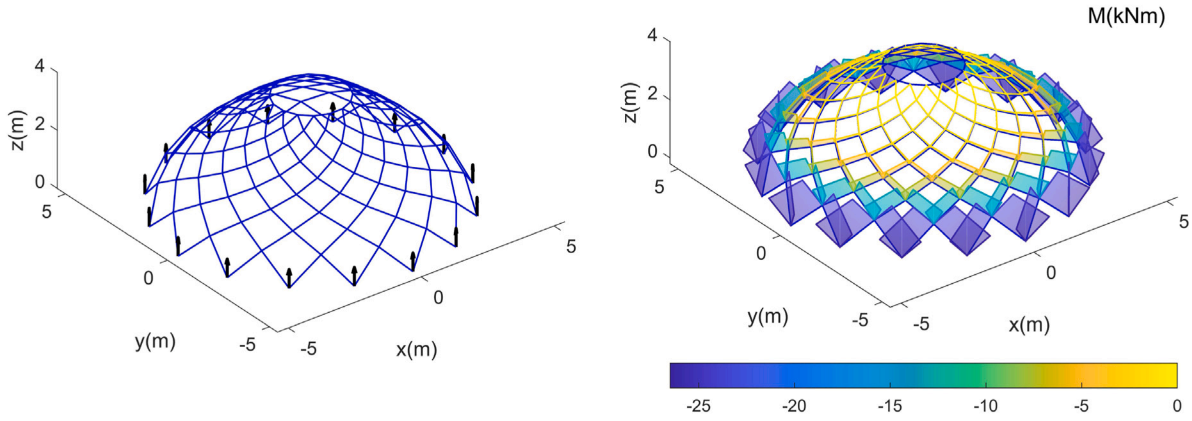

Fig. 16. EFDM design of a gridshell dome with oculus: shape, force reactions and bending moment diagram.

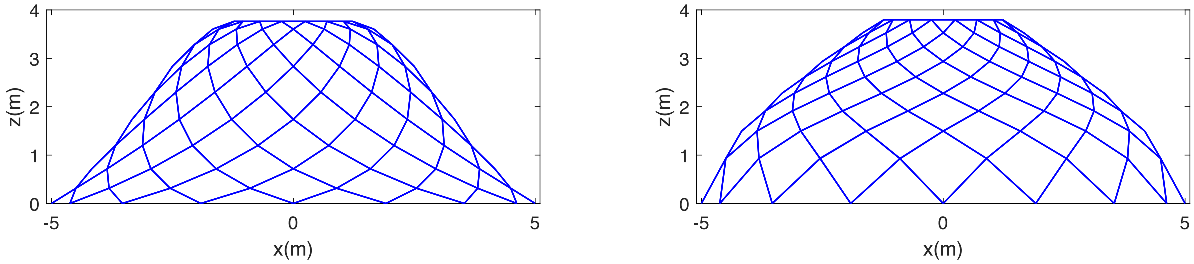

Fig. 17. Design of a gridshell dome with oculus: lateral view comparing the FDM layout (left) and the EFDM layout (right).

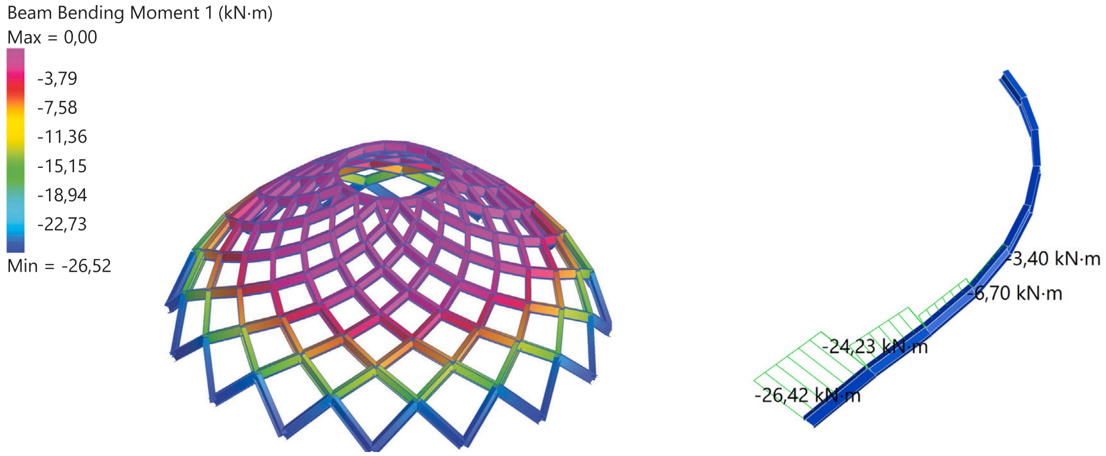

Fig. 18. EFDM design of a gridshell dome with oculus: bending moment representation (color map for the structure and diagram for a part), as obtained through finite-element analysis.

equal to 4.30 kN. In the bending moment diagram, hogging moments are distributed along all cantilevered spiral branches of the structure. Their intensity increases from the apex toward the supports, where they accumulate into moment reactions transmitted to the ground. By vectorially summing the moments at the ends of the branches converging at the same restrained node, a resultant radial moment reaction is obtained, equal to 26.05 kNm.

The geometry of the thrust-free EFDM layout differs significantly from that of the FDM funicular network. A side-view comparison is provided in Fig. 17.

To verify the moment distribution presented in Fig. 16, finite element analyses were performed [58]. IPE 240 cross-sections were adopted for all members of the grid, with the web oriented vertically, and end releases were introduced to model connections that do not allow the transfer of torsion and moments in the horizontal loading plane. Structural steel (S275) was assumed in the simulation. A linear elastic analysis was carried out by applying, at the n inner nodes, the point forces used as input in the optimization process, and at the n_f nodes along the perimeters, vertical point forces equal to 4.30 kN and radial moments 26.05 kNm (i.e. the force and moment reactions computed in the EFDM solution). In Fig. 18, the bending moments retrieved from the finite element solution are shown: a color map of the entire dome is provided along with the bending moment diagram for a spiral branch. A very good agreement was observed between the EFDM result (peak value 26.50 kNm) and the finite element analysis (peak value 26.52 kNm). It is worth noting that the same result was achieved by performing a linear elastic analysis of the structure in which all loads were removed from the n_f nodes along the perimeter and replaced by displacement boundary conditions prescribing zero vertical displacements and rotations. Hence, the internal moments given in Fig. 16 correspond to the stress state of the gridshell dome supported by elements capable of sustaining only vertical forces and (radial) moments.

A final remark relevant to the entire set of simulations reported in Section 3 concerns the adoption of the aggregation function in Eq. 19, used with $\rho = 100$, as the objective function to provide a smooth approximation of r_{max}. For each optimization run, Table 1 reports both the peak value of the force reaction r_{max} and the value of the objective function at convergence f_c, with a relative error consistently smaller than 0.5%.

4. Conclusion

An extended formulation of the force density method has been introduced to address the equilibrium-based form-finding of gridshells with a fixed footprint that exhibit bending resistance in the vertical plane.

Considering the effect of point forces applied at the nodes of the reticulated shell, constant shear forces and linearly varying bending moments can develop within the members, in addition to the constant axial forces typical of funicular networks. In this context, the “shear force density“ has been defined as the ratio between the shear force induced by the bending moment at one end of the member and its length. Upon introduction of the axial and shear force densities, the translational equilibrium of the nodes has been shown to remain linear in the vertical coordinates, provided the gridshell has fixed footprint.

A min–max optimization problem has been defined over the two sets of force densities, aiming to identify – among the reticulated shells that satisfy equilibrium within a prescribed plan projection – those configurations constrained to a prescribed total length that minimize the magnitude of the reaction forces at the restrained nodes. Vertical translational equilibrium has been used to determine the elevation of unrestrained nodes, while equality constraints have been imposed to enforce both rotational equilibrium and horizontal translational equilibrium. An interior-point approach has been employed to address the emerging multi-constrained optimization problem, adopting a smooth aggregation to approximate the maximum function. Matrix-based expressions for sensitivity analysis have been derived.

Numerical simulations have been carried out to explore, within the same formulation, both funicular networks and bending-resistant layouts. By adjusting the side constraints on shear force densities, expressed as the bending moments at the branch ends divided by the square of their length, it is possible to control the bending resistance of the hybrid truss-beam branches in the arising solution. The funicular configurations emerge as special cases when the side constraints on shear force densities are set to zero. All the results obtained satisfy both translational and rotational equilibrium at the unrestrained nodes, and exhibit a uniform distribution of reaction forces at the restrained nodes. Examples of bending-resistant arches, arch grids, and gridshell domes have been presented, highlighting equilibrated solutions that transmit gravity loads without requiring horizontal reactions. The applicability of the proposed framework and the physical validity of the retrieved stress states have been discussed.

Differently from a ground-structure approach, see e.g. [38], the proposed method does not search for feasible solutions within a prescribed set of bar layouts, but instead allows for a continuous variation of the vertical coordinates of the nodes. Rather than performing topology optimization in conjunction with geometry projection to recover straight bars, see e.g. [53], the desired geometrical entities are directly handled in the adopted optimization approach, addressing hybrid truss-beam members. In its current version, the implemented formulation does not allow for seeking the optimal distribution of cross-sections of hybrid members across the gridshells. An a posteriori member sizing procedure should be applied to ensure the required resistance based on the retrieved stress state, see also the methods discussed in [5,13]. However, the proposed approach could be conveniently extended to incorporate the optimal design of cross-sectional areas as additional variables within the same minimization framework.

The ongoing research primarily focuses on enhancing the proposed formulation by introducing local constraints to strictly control the allowable bending moments in the branches of the reticulated shells, while progressing toward the aforementioned extension of the framework to optimize both geometry and topology of hybrid truss-beam gridshells.

CRediT authorship contribution statement

Ferdinando Auricchio: Conceptualization, Supervision. **Matteo Bruggi:** Methodology, Software. **Bálint Tóth:** Investigation, Data Curation.

Declaration of competing interest

The authors declare that they have no known competing financial interests or personal relationships that could have appeared to influence the work reported in this paper.

Acknowledgments

The second author was funded by the European Union - Next Generation EU, Mission 4, Component 1, CUP D53D23003900006, PRIN 2022P7FLNC “LATTICE” (Lattice meso-elements for a new class of green steel structures).

The third author was funded by the Ministry of Culture and Innovation of Hungary - National Research, Development and Innovation Found, EKÖP_KDP-24-1-BME-24 funding scheme.

Appendix. Sensitivity computation

Dealing with funicular networks, the sensitivity computation with respect to the force densities in $\mathbf{q}$ was originally provided in [9] for the vectors gathering the coordinates of the nodes, $\mathbf{x}$, $\mathbf{y}$, $\mathbf{z}$, and the length of the bars, $\mathbf{l}$. The adopted procedure can be straightforwardly extended to the computation of Jacobian matrices for reticulated shells with fixed footprint that are bending-resistant in the vertical plane. Addressing the third block of Eqs. 12, and enforcing that any changes $d\mathbf{q}$, $d\mathbf{m}_1$, $d\mathbf{m}_2$, and $d\mathbf{z}$ do not affect the state of equilibrium, one has:

$$\frac{\partial \mathbf{z}}{\partial \mathbf{q}} = (\mathbf{C}^T\mathbf{Q}\mathbf{C})^{-1}(-\mathbf{C}^T\mathbf{W}), \quad \frac{\partial \mathbf{z}}{\partial \mathbf{m}_1} = (\mathbf{C}^T\mathbf{Q}\mathbf{C})^{-1}(\mathbf{C}^T(\mathbf{U}^2+\mathbf{V}^2)\mathbf{L}_{xy}^{-1}), \quad \frac{\partial \mathbf{z}}{\partial \mathbf{m}_2} = -\frac{\partial \mathbf{z}}{\partial \mathbf{m}_1}, \tag{A.1}$$

where $\partial\mathbf{w}/\partial\mathbf{z} = \mathbf{C}_z$ has been used, see Eq. (1), as well as the assumption of design-independent loads. Then, one has:

$$\frac{\partial \mathbf{l}}{\partial \mathbf{q}} = \frac{\partial \mathbf{l}}{\partial \mathbf{z}}\frac{\partial \mathbf{z}}{\partial \mathbf{q}} = \mathbf{L}^{-1}\mathbf{W}\mathbf{C}\frac{\partial \mathbf{z}}{\partial \mathbf{q}}, \quad \frac{\partial \mathbf{l}}{\partial \mathbf{m}_1} = \frac{\partial \mathbf{l}}{\partial \mathbf{z}}\frac{\partial \mathbf{z}}{\partial \mathbf{m}_1}, \quad \frac{\partial \mathbf{l}}{\partial \mathbf{m}_2} = \frac{\partial \mathbf{l}}{\partial \mathbf{z}}\frac{\partial \mathbf{z}}{\partial \mathbf{m}_2}. \tag{A.2}$$

The sensitivity of the constraints and of the objective function in Eq. (15) can be found exploiting matrix differentiation and the above results.

Upon introduction of $\mathbf{M}_1 = \text{diag}(\mathbf{m}_1)$ and $\mathbf{M}_2 = \text{diag}(\mathbf{m}_2)$, the sensitivity of the l.h.s of Eq. (15c), herein denoted by $\mathbf{g}_1$, may be written as:

$$\begin{aligned}
\frac{\partial \mathbf{g}_1}{\partial \mathbf{q}} &= \mathbf{C}^T\mathbf{U} - \mathbf{C}^T\mathbf{U}\mathbf{L}_{xy}^{-1}(\mathbf{M}_2-\mathbf{M}_1)\mathbf{C}\frac{\partial \mathbf{z}}{\partial \mathbf{q}},\\
\frac{\partial \mathbf{g}_1}{\partial \mathbf{m}_1} &= \mathbf{C}^T\mathbf{U}\mathbf{L}_{xy}^{-1}\mathbf{W} - \mathbf{C}^T\mathbf{U}\mathbf{L}_{xy}^{-1}(\mathbf{M}_2-\mathbf{M}_1)\mathbf{C}\frac{\partial \mathbf{z}}{\partial \mathbf{m}_1},\\
\frac{\partial \mathbf{g}_1}{\partial \mathbf{m}_2} &= -\mathbf{C}^T\mathbf{U}\mathbf{L}_{xy}^{-1}\mathbf{W} - \mathbf{C}^T\mathbf{U}\mathbf{L}_{xy}^{-1}(\mathbf{M}_2-\mathbf{M}_1)\mathbf{C}\frac{\partial \mathbf{z}}{\partial \mathbf{m}_2}.
\end{aligned} \tag{A.3}$$

Using $\mathbf{V}$ instead of $\mathbf{U}$ in above equations, one gets the sensitivity of the l.h.s of Eq. (15d). The derivatives of the l.h.s of Eq. (15e), herein denoted by $\mathbf{g}_3$, may be written as:

$$\begin{aligned}
\frac{\partial \mathbf{g}_3}{\partial \mathbf{q}} &= 2\mathbf{C}_1^T\mathbf{V}\mathbf{L}_{xy}^{-1}\mathbf{M}_1\mathbf{L}\frac{\partial \mathbf{l}}{\partial \mathbf{q}} + 2\mathbf{C}_2^T\mathbf{V}\mathbf{L}_{xy}^{-1}\mathbf{M}_2\mathbf{L}\frac{\partial \mathbf{l}}{\partial \mathbf{q}},\\
\frac{\partial \mathbf{g}_3}{\partial \mathbf{m}_1} &= \mathbf{C}_1^T\mathbf{V}\mathbf{L}_{xy}^{-1}\mathbf{L}^2 + 2\mathbf{C}_1^T\mathbf{V}\mathbf{L}_{xy}^{-1}\mathbf{M}_1\mathbf{L}\frac{\partial \mathbf{l}}{\partial \mathbf{m}_1} + 2\mathbf{C}_2^T\mathbf{V}\mathbf{L}_{xy}^{-1}\mathbf{M}_2\mathbf{L}\frac{\partial \mathbf{l}}{\partial \mathbf{m}_1},\\
\frac{\partial \mathbf{g}_3}{\partial \mathbf{m}_2} &= \mathbf{C}_2^T\mathbf{V}\mathbf{L}_{xy}^{-1}\mathbf{L}^2 + 2\mathbf{C}_1^T\mathbf{V}\mathbf{L}_{xy}^{-1}\mathbf{M}_1\mathbf{L}\frac{\partial \mathbf{l}}{\partial \mathbf{m}_2} + 2\mathbf{C}_2^T\mathbf{V}\mathbf{L}_{xy}^{-1}\mathbf{M}_2\mathbf{L}\frac{\partial \mathbf{l}}{\partial \mathbf{m}_2}.
\end{aligned} \tag{A.4}$$

Using $\mathbf{U}$ instead of $\mathbf{V}$ in above equations, one has the sensitivity of the l.h.s of Eq. (15f).

Similarly, the sensitivity of the vectors $\mathbf{r}_x$, $\mathbf{r}_y$, $\mathbf{r}_z$ can be found by working on Eq. (18). Reference is made to [54] for the derivative of the aggregation function $J_{KS}(\mathbf{r})$ of Eq. (19).

Data availability

Data will be made available on request.

References

[1] Adriaenssens S, Block P, Veenendaal D, Williams CJK. Shell structures for architecture: Form finding and optimization. Routledge; 2014.

[2] Veenendaal D, Block P. An overview and comparison of structural form finding methods for general networks. Int J Solids Struct 2012;49(26):3741–53.

[3] Winslow P, Pellegrino S, Sharma SB. Multi-objective optimization of free-form grid structures. Struct Multidiscip Optim 2010;40(1–6):257–69.

[4] Richardson JN, Adriaenssens S, Filomeno Coelho R, Bouillard P. Coupled form-finding and grid optimization approach for single layer grid shells. Eng Struct 2013;52:230–9.

[5] Jiang Y, Zegard T, Baker WF, Paulino GH. Form-finding of grid-shells using the ground structure and potential energy methods: a comparative study and assessment. Struct Multidiscip Optim 2018;57(3):1187–211.

[6] Rombouts J, Lombaert G, De Laet L, Schevenels M. A novel shape optimization approach for strained gridshells: Design and construction of a simply supported gridshell. Eng Struct 2019;192:166–80.

[7] Manuello A. Multi-body rope approach for grid shells: Form-finding and imperfection sensitivity. Eng Struct 2020;221:111029.

[8] Chovghi F, Richter C, D'Acunto P. Fabrication-aware structural form-finding for additive manufacturing: An equilibrium-based approach. Autom Constr 2025;178(106386):106386.

[9] Schek H. The force density method for form finding and computation of general networks. Comput Methods Appl Mech Engrg 1974;3(1):115–34.

[10] Greco L, Cuomo M. On the force density method for slack cable nets. Int J Solids Struct 2012;49(13):1526–40.

[11] Malerba PG, Patelli M, Quagliaroli M. An extended force density method for the form finding of cable systems with new forms. Struct Eng Mech 2012;42(2):191–210.

[12] Maurin B, Motro R. The surface stress density method as a form-finding tool for tensile membranes. Eng Struct 1998;20(8):712–9.

[13] Ohsaki M, Hayashi K. Force density method for simultaneous optimization of geometry and topology of trusses. Struct Multidiscip Optim 2017;56(5):1157–68.

[14] Hayashi K, Ohsaki M. FDMopt: Force density method for optimal geometry and topology of trusses. Adv Eng Softw 2019;133:12–9.

[15] Vassart N, Motro R. Multiparametered formfinding method: application to tensegrity systems. Int J Space Struct 1999;14(2):147–54.

[16] Zhang J, Ohsaki M. Adaptive force density method for form-finding problem of tensegrity structures. Int J Solids Struct 2006;43(18–19):5658–73.

[17] Xu X, Wang Y, Luo Y. Finding member connectivities and nodal positions of tensegrity structures based on force density method and mixed integer nonlinear programming. Eng Struct 2018;166:240–50.

[18] Zhang L-Y, Zhu S-X, Li S-X, Xu G-K. Analytical form-finding of tensegrities using determinant of force-density matrix. Compos Struct 2018;189:87–98.

[19] Liew A, Avelino R, Moosavi V, Van Mele T, Block P. Optimising the load path of compression-only thrust networks through independent sets. Struct Multidiscip Opt 2019;60(1):231–44.

[20] Gade J, Geiger F, Kemmler R, Bischoff M. A form-finding method for adaptive truss structures subject to multiple static load cases. Int J Space Struct 2024;39(2):93–114.

[21] Gao J, Chen M, Wang Y, Yang Z, Tang L, Xu P, Chen W. Force density method's energy principle and application in membrane-cable-strut-beam hybrid structures. J Build Eng 2025;99:111523.

[22] Pauletti RMO, Pimenta PM. The natural force density method for the shape finding of taut structures. Comput Methods Appl Mech Engrg 2008;197(49–50):4419–28.

[23] Guerra Riaño AF, Várkonyi PL. Form-finding using the force density method: Existence of solutions, singularities, and an analogy to electric circuits. Int J Space Struct 2023;38(4):302–26.

[24] Descamps B, Filomeno Coelho R, Ney L, Bouillard P. Multicriteria optimization of lightweight bridge structures with a constrained force density method. Comput Struct 2011;89(3–4):277–84.

[25] Morterolle S, Maurin B, Quirant J, Dupuy C. Numerical form-finding of geotensoid tension truss for mesh reflector. Acta Astronaut 2012;76:154–63.

[26] Yuan S, Yang B. The fixed nodal position method for form finding of high-precision lightweight truss structures. Int J Solids Struct 2019;161:82–95.

[27] Christensen PW, Klarbring A. An introduction to structural optimization. Solid mechanics and its applications, vol. 153, Dordrecht, Netherlands: Springer; 2008, p. 1–220.

[28] Block P, Lachauer L. Three-dimensional funicular analysis of masonry vaults. Mech Res Commun 2014;56:53–60.

[29] Bruggi M. A constrained force density method for the funicular analysis and design of arches, domes and vaults. Int J Solids Struct 2020;193–194:251–69.

[30] Nodargi NA, Bisegna P. Generalized thrust network analysis for the safety assessment of vaulted masonry structures. Eng Struct 2022;270:114878.

[31] Chianese C, Rosati L, Marmo F. Isogeometric form finding of membrane shells by optimised airy stress function. Comput Methods Appl Mech Engrg 2024;426(116946):116946.

[32] Baker WF, Beghini LL, Mazurek A, Carrion J, Beghini A. Maxwell2019s reciprocal diagrams and discrete michell frames. Struct Multidiscip Optim 2013;48(2):267–77.

[33] Kirsch U. Structural optimization: Fundamentals and applications. Berlin, Germany: Springer; 1993.

[34] Liew A. Constrained force density method optimisation for compression-only shell structures. Structures 2020;28:1845–56.

[35] Bruggi M, Laghi V, Trombetti T. Stress-based form-finding of gridshells for wire-and-arc additive manufacturing considering overhang constraints. Eng Struct 2023;279:115654.

[36] Gilbert M, Tyas A. Layout optimization of large-scale pin-jointed frames. Eng Comput 2003;20:1044–64.

[37] Sokół T. A 99 line code for discretized michell truss optimization written in mathematica. Struct Multidiscip Opt 2011;43(2):181–90.

[38] Zegard T, Paulino GH. GRAND3 — Ground structure based topology optimization for arbitrary 3D domains using MATLAB. Struct Multidiscip Opt 2015;52(6):1161–84.

[39] Skelton RE, de Oliveira MC. Optimal tensegrity structures in bending: The discrete michell truss. J Franklin Inst 2010;347(1):257–83.

[40] Bai X, Chen M. Lightweight design of tensegrity michell truss subject to cantilever loads. Compos Struct 2025;357:118925.

[41] Bolbotowski K, He L, Gilbert M. Design of optimum grillages using layout optimization. Struct Multidiscip Opt 2018;58(3):851–68.

[42] Lu H, He L, Gilbert M, Tyas A. Plastic layout optimization of hybrid truss and beam structures. Struct Multidiscip Optim 2025;68(3).

[43] Laccone F, Pietroni N, Cignoni P, Malomo L. Bending-reinforced grid shells for free-form architectural surfaces. Comput Aided Des 2024;168(103670):103670.

[44] Bletzinger K-U, Ramm E. Structural optimization and form finding of light weight structures. Comput Struct 2001;79(22–25):2053–62.

[45] Rombouts J, Liew A, Lombaert G, De Laet L, Block P, Schevenels M. Designing bending-active gridshells as falsework for concrete shells through numerical optimization. Eng Struct 2021;240:112352.

[46] Palmieri M, Giannetti I, Micheletti A. Floating-bending tensile-integrity structures. Curved Layer Struct 2021;8(1):89–95.

[47] Rimoli JJ, Garanger K, Ruffini F. Flexible tensegrity structures: From space applications to 3D tensegrity metamaterials. In: CISM international centre for mechanical sciences. Cham: Springer Nature Switzerland; 2025, p. 101–28.

[48] Zhang J, Ohsaki M, Rimoli JJ, Kogiso K. Optimization for energy absorption of 3-dimensional tensegrity lattice with truncated octahedral units. Compos Struct 2021;267(113903):113903.

[49] Nocedal J, Wright S. Numerical optimization. 2nd ed. New York, NY: Springer; 2006.

[50] Kreisselmeier G, Steinhauser R. Systematic control design by optimizing a vector performance index. In: Computer aided design of control systems. Elsevier; 1980, p. 113–7.

[51] Fin J, Borges LA, Fancello EA. Structural topology optimization under limit analysis. Struct Multidiscip Optim 2019;59(4):1355–70.

[52] Inc. TM. Optimization Toolbox version: 25.1 (R2025a). Natick, Massachusetts, United States: The MathWorks Inc.; 2025, Available from: https://www.mathworks.com.

[53] Smith H, Norato JA. A MATLAB code for topology optimization using the geometry projection method. Struct Multidiscip Optim 2020;62(3):1579–94.

[54] Ferrari F, Sigmund O, Guest JK. Topology optimization with linearized buckling criteria in 250 lines of matlab. Struct Multidiscip Optim 2021;63(6):3045–66.

[55] Gravesen J, Evgrafov A, Nguyen DM. On the sensitivities of multiple eigenvalues. Struct Multidiscip Optim 2011;44(4):583–7.

[56] Raspanti CG, Bandoni JA, Biegler LT. New strategies for flexibility analysis and design under uncertainty. Comput Chem Eng 2000;24(9–10):2193–209.

[57] Lewiński T, Sokół T, Graczykowski C. Michell structures. Cham: Springer; 2019.

[58] Strand7, release 3. Strand7 Pty Ltd; 2021, Available from: www.strand7.com/r3.

[59] Gythiel W, Mommeyer C, Raymaekers T, Schevenels M. A comparative study of the structural performance of different types of reticulated dome subjected to distributed loads. Front Built Env 2020;6.

[60] Meng L, Zhang J, Hou Y, Breitkopf P, Zhu J, Zhang W. Revisiting the fibonacci spiral pattern for stiffening rib design. Int J Mech Sci 2023;246:108131.